Suppression of transcytosis regulates zebrafish blood-brain barrier development

Natasha M. O'Brown[1], Sean G. Megason[2*], Chenghua Gu[1*]

[1] Department of Neurobiology, [2] Department of Systems Biology, Harvard Medical School, 220 Longwood Ave, Boston, MA 02115, U.S.A.

* denotes corresponding author

Correspondence:

Chenghua Gu (chenghua_gu@hms.harvard.edu)

Department of Neurobiology, Harvard Medical School

Boston, MA 02115, U.S.A.

(Phone) 617-432-6364 (Fax) 617-432-1639

Sean Megason (sean_megason@hms.harvard.edu)

Department of Systems Biology, Harvard Medical School

Boston, MA 02115, U.S.A.

(Phone) 617-432-7441

Abstract:

As an optically transparent model organism with an endothelial blood-brain barrier (BBB), zebrafish offer a powerful tool to study the vertebrate BBB. However, the precise developmental profile of functional zebrafish BBB acquisition and the subcellular and molecular mechanisms governing the zebrafish BBB remain poorly characterized. Here we find a spatiotemporal gradient of barrier acquisition. Moreover, we capture the dynamics of developmental BBB leakage using live imaging, revealing a combination of steady accumulation in the parenchyma and sporadic bursts of tracer leakage. Electron microscopy studies further reveal that this steady accumulation results from high levels of transcytosis that are eventually suppressed, sealing the BBB. Finally, we demonstrate a key mammalian BBB regulator Mfsd2a, which inhibits transcytosis, plays a conserved role in zebrafish. *Mfsd2aa* mutants display increased larval and adult BBB permeability due to increased transcytosis. Our findings indicate a conserved developmental program of barrier acquisition between zebrafish and mice.

Introduction

Blood vessels in the vertebrate brain are composed of a single layer of endothelial cells that possess distinct functional properties that allow the passage of necessary nutrients yet prevent unwanted entry of specific toxins and pathogens into the brain. This specialized endothelial layer forms the blood-brain barrier (BBB) and restricts the passage of substances between the blood and the brain parenchyma via two primary mechanisms: 1) specialized tight junction complexes between apposed endothelial cells to prevent intercellular transit (Reese and Karnovsky, 1967; Brightman and Reese, 1969) and 2) suppressing vesicular trafficking or transcytosis to prevent transcellular transit (Ben-Zvi et al., 2014; Andreone et al., 2015; Andreone et al., 2017). BBB selectivity is further refined with expression of substrate-specific transporters that dynamically regulate the influx of necessary nutrients and efflux of metabolic waste products (Sanchez-Covarrubias et al., 2014). While the BBB is comprised of endothelial cells, the surrounding perivascular cells including pericytes and astroglial cells, play a critical role in forming and maintaining barrier properties (Janzer and Raff, 1987; Armulik et al., 2010; Bell et al., 2010; Daneman et al., 2010; Wang et al., 2014). Collectively, endothelial cells and the surrounding perivascular cells form the neurovascular unit.

As the simplest genetic model organism with an endothelial BBB (Jeong et al., 2008), zebrafish offer a powerful tool to study the cellular and molecular properties of the vertebrate BBB (Xie et al., 2010; Vanhollebeke et al., 2015; Umans et al., 2017; O'Brown et al., 2018; Quiñonez-Silvero et al., 2019). Zebrafish have served as a great model system to study vascular biology due to their large clutch size, rapid and external development, and transparency for *in vivo* whole organism live-imaging (Jin et al., 2005; Santoro et al., 2007; Armer et al., 2009; Herbert et al., 2009; Phng et al., 2009; Geudens et al., 2010; Herbert et al., 2012; Wilkinson and van Eeden, 2014; Franco et al., 2015; Vanhollebeke et al., 2015; Matsuoka et al., 2016; Geudens et al., 2018). Additionally, with the advent of CRISPR-Cas9 technology, zebrafish provide an efficient genetic

63 toolkit for targeted mutagenesis (Hwang et al., 2013; Gagnon et al., 2014; Ablain et al., 2015;
64 Varshney et al., 2015; Albadri et al., 2017; Hogan and Schulte-Merker, 2017). However, the
65 subcellular and molecular mechanisms governing the formation and maintenance of the zebrafish
66 BBB remain poorly characterized. Expanding our understanding of the zebrafish BBB can thus
67 reveal the mechanistic similarities between the zebrafish and mammalian BBB to further elevate
68 the position of zebrafish as a model organism for studying the BBB.
69
70 Barrier properties of brain endothelial cells are induced by extrinsic signals from other cells in the
71 surrounding microenvironment during development (Stewart and Wiley, 1981). In rodents, the
72 BBB becomes functionally sealed in a spatiotemporal gradient, with the hindbrain and midbrain
73 barriers becoming functional before the cortical barrier (Daneman et al., 2010; Ben-Zvi et al.,
74 2014). Within the cortex, barrier function is acquired along a ventral-lateral to dorsal-medial
75 gradient (Ben-Zvi et al., 2014). In the zebrafish, existing studies have disagreed over the timing
76 of zebrafish barrier formation, with some suggesting that BBB maturation occurs at 3 days post
77 fertilization (dpf) (Jeong et al., 2008; Umans et al., 2017) and others providing a wide range
78 beginning at 3 dpf and extending to 10 dpf (Fleming et al., 2013). These conflicting reports may
79 be due to regional developmental gradients of barrier acquisition or differences in the
80 experimental approaches used to assess BBB permeability such as the molecular weight of
81 tracers and circulation time. To date, a thorough regional characterization of functional barrier
82 acquisition has been lacking in zebrafish.
83
84 Recent work in the mammalian blood-retinal barrier has indicated that suppression of transcytosis
85 governs functional barrier development (Chow and Gu, 2017). Interestingly endothelial cells at
86 the leaky neonatal angiogenic front possess functional tight junction complexes halting the
87 intercellular passage of the tracer protein Horseradish Peroxidase (HRP) at the so-called “kissing
88 points”. In contrast, these endothelial cells exhibit high levels of HRP-filled vesicles compared to

89 functionally sealed proximal vessels. Moreover, these areas of elevated vesicular trafficking
90 continue to correspond with barrier permeability at the angiogenic front until the barrier seals
91 (Chow and Gu, 2017). Work in the mouse BBB has also demonstrated the importance of
92 suppressing transcytosis in determining barrier permeability. Mice lacking the major facilitator
93 super family domain containing 2a (Mfsd2a) lipid transporter exhibit increased levels of caveolae
94 vesicles in CNS endothelial cells, resulting in increased barrier permeability (Ben-Zvi et al., 2014;
95 Andreone et al., 2017). The subcellular and molecular mechanisms of zebrafish BBB acquisition
96 have yet to be elucidated.
97
98 Here in zebrafish, we find a spatiotemporal gradient of barrier acquisition, and capture the
99 dynamics of developmental BBB leakage using time lapse live imaging. We further find a
100 conserved role for transcytosis suppression in determining barrier properties, both during normal
101 development and in *mfsd2aa* mutants.
102
103 **Results**
104 *Posterior-Anterior Gradient of Zebrafish BBB Development*
105 To determine when and how the zebrafish BBB becomes functional in different brain regions, we
106 performed intracardiac injections of fluorescently-conjugated tracers (1 kDa NHS and 10 kDa
107 Dextran) simultaneously at different developmental stages and imaged live fish after one hour of
108 tracer circulation (Figure 1A and 1B). We used a combination of different molecular weight tracers
109 to tease apart potential avenues of leakage, as tight junctional defects result specifically in the
110 leakage of low molecular weight tracers 1 kDa and below into the brain parenchyma (Nitta et al.,
111 2003; Campbell et al. 2008; Sohet et al., 2015; Yanagida et al. 2017). At 3 dpf, we observed a
112 sealed barrier in the hindbrain as previously described (Jeong et al., 2008), with only a few of the
113 parenchymal cells taking up the injected tracer (average of 2 ± 0.3 cells/embryo with NHS and 2
114 ± 0.4 cells/embryo with Dextran; Figure 1 – Supplement 1), which we quantify as a proxy of tracer

115 leakage into the brain. However, in the midbrain we observed an increased number of
116 parenchymal cells that accumulated the circulating tracers (average of 24 ± 1 cells/embryo with
117 NHS and 24 ± 1 cells/embryo with Dextran; Figure 1C and 1D), indicating that the tracers leaked
118 out of the blood vessels into the brain and that the midbrain barrier is not yet functional. In addition
119 to the use of exogenous injected fluorescent tracers, we also assayed BBB permeability with an
120 endogenous transgenic serum DBP-EGFP fusion protein (Tg(*l-fabp:DBP-EGFP*)) to account for
121 injection artifacts (Xie et al., 2010). At 3 dpf, we observed similar leakage patterns with the
122 transgenic serum protein as we did with the injected tracers (average of 24 ± 1 cells/embryo in
123 the midbrain and average of 2 ± 0.4 cells/embryo in the hindbrain; Figure 1C and D; Figure 1 –
124 Supplement 1). At 4 dpf, the BBB in the hindbrain is completely functional with few tracer-filled
125 parenchymal cells (average of 3 ± 0.4 cells/embryo with NHS, 2 ± 0.4 cells/embryo with Dextran
126 and DBP-EGFP; Figure 1 – Supplement 1). However, the midbrain BBB remains leaky (average
127 of 23 ± 1 cells/embryo with NHS and DBP-EGFP and 24 ± 1 cells/embryo with Dextran; $p=0.68$
128 compared to 3 dpf, one-way ANOVA; Figure 1C and 1D). However, at 5 dpf the number of
129 midbrain parenchymal cells that uptake the tracers is dramatically reduced (average of 9 ± 1
130 cells/embryo with NHS, Dextran, and DBP-EGFP; $p<0.0001$, one-way ANOVA; Figure 1B and
131 1C) and no change was observed in the hindbrain (Figure 1 – Supplement 1). No significant
132 change was observed in midbrain permeability from 5 to 6 dpf (average of 8 ± 1 cells/embryo with
133 NHS, Dextran, and DBP-EGFP; $p=0.904$, one-way ANOVA; Figure 1C and 1D), indicating that
134 the midbrain barrier becomes sealed at 5 dpf. We did not assay the forebrain at any of these
135 stages due to the fact that it remains avascularized until 5 dpf. Of note, all three tracers showed
136 nearly indistinguishable patterns of uptake, with similar numbers of cells and many of the same
137 cells simultaneously taking up both injected tracers (Figure 1; Figure 1 – Supplement), suggesting
138 that the leakage is not due to tight junctional defects but may rather be due to an increase in
139 vesicular trafficking.

140 *Time lapse Imaging Reveals Two Modes of Developmental Leakage*

141 The vast majority of studies interrogating BBB permeability have relied on observing leakage in
142 fixed static images from mutant mice, which does not reveal the dynamic nature of the BBB. A
143 huge advantage of zebrafish is the ability to examine biological processes *in vivo* in real-time,
144 providing us with the unique opportunity to observe the process of BBB maturation (Figure 1). To
145 examine the developmental dynamics of barrier leakage, we injected embryos at 3 dpf with
146 fluorescently-labeled 10 kDa Dextran and performed time lapse live imaging for an hour following
147 injection, with time 0 being an average of 8 minutes post-injection. We observed a gradual and
148 diffuse increase in extravascular Dextran intensity over time within the brain parenchyma (slope
149 of 1.301e-4 intensity/sec; Videos 1 and 2; Figure 2A, 2C and 2E). In addition to the time-
150 dependent increase in overall Dextran intensity in the brain parenchyma, we also observed
151 parenchymal cells taking up tracer, both directly adjacent to blood vessels and at a small distance
152 away (Figure 2A and 2C), as in the static images of tracer leakage during development (Figure
153 1). Interestingly, at 3 dpf we observed an actively sprouting cell that extended away from the
154 established vessel in a sporadic fashion (Video 2; Figure 2A). After twenty minutes of rambling
155 migration, this sprout suddenly released a large bolus of Dextran that appeared to be taken up by
156 a single parenchymal cell. Two minutes later, this same sprout released a second bolus of Dextran
157 on the opposite side (Video 2). These rare large bursts of leakage were not unique to this sprout;
158 they were also sporadically observed from established blood vessels (Video 1; Figure 2A). This
159 data revealed two types of leakage occurring during this early developmental stage: steady and
160 diffuse Dextran leakage into the parenchyma that makes up the vast majority of observed leakage
161 and rare large bursts of leakage. When we performed these same time lapse experiments at 5
162 dpf, we observed significantly less overall tracer accumulation in the brain parenchyma over the
163 course of the hour in addition to reduced rates of tracer accumulation (slope of 4.641e-5
164 intensity/sec; Video 3; $p<0.001$, Mann-Whitney test; Figure 2B, 2D and 2E). Furthermore, 5 dpf
165 fish never exhibited bursts of tracer leakage as observed at 3 dpf. Overall, 5 dpf fish had far fewer

166 parenchymal cells filling with Dextran than at 3 dpf, as observed in the static tracer leakage assays
167 (Figure 1). We interpret these data to suggest that at early stages, most tracer leakage occurs
168 broadly through vessel walls potentially via unrestricted transcytosis with an occasional transient
169 rupture to endothelial integrity that lead to these large bursts of leakage. Once tracer is leaked
170 into the intercellular space of the parenchyma it is taken up by select parenchymal cells. As the
171 BBB matures both sources of leakage sharply decrease.
172
173 *Suppression of Transcytosis Governs BBB Development*
174 Given the observed differences in permeability during larval development, we next sought to
175 determine the subcellular mechanisms underlying the development of a functional BBB.
176 Therefore, we assessed BBB properties by performing intracardiac injections of electron-dense
177 NHS-gold nanoparticles (5 nm) followed by transmission electron microscopy (TEM) at different
178 developmental stages when the midbrain barrier is leaky (3 dpf) and when it is functionally sealed
179 to fluorescent tracers (5 and 7 dpf; Figure 3). All of the blood vessels analyzed had a maximal
180 diameter of 5 μm to enrich for capillaries and small veins. At 3 dpf, we found blood vessels in
181 direct contact with neurons and pericytes, with the pericytes sharing the endothelial basement
182 membrane (Figure 3A), as in the mammalian neurovascular unit. During this leaky developmental
183 stage, the endothelial basement membrane was filled with the electron-dense gold nanoparticles
184 (Figure 3A and 3B; turquoise arrowheads) with an average gold intensity of 1.29 ± 0.07 (luminal
185 gold intensity normalized to 1.0; Figure 3G), further demonstrating that the BBB is immature at 3
186 dpf. To decipher how the gold nanoparticles traverse from the lumen to the basement membrane,
187 we first looked at the tight junctions to see if the nanoparticles passed between apposed
188 endothelial cells. After careful examination, we observed that the nanoparticles were halted at the
189 "kissing points" between endothelial cells, indicating that tight junctions were functional prior to
190 formation of a functional BBB (49/49 functional tight junctions; Figure 3B; green arrowhead). As
191 transcytosis has been implicated in the maturation of the blood-retinal barrier (Chow and Gu,

192 2017), we next examined the levels of luminal and abluminal flask-shaped vesicles filled with gold
193 nanoparticles as a means of assessing transcytosis. Quantification of gold-filled luminal and
194 abluminal flask-shaped vesicles revealed an average of 0.21 ± 0.03 and 0.17 ± 0.02 vesicles/μm,
195 respectively (Figure 3H and 3I). These data reveal that the basement membrane becomes filled
196 with gold nanoparticles via vesicular transport rather than intercellular passage between immature
197 tight junctions.
198
199 When we repeated this assay at 5 dpf, when the barrier becomes less permeable to fluorescently
200 conjugated tracers (Figures 1 and 2), we still observe close contacts between endothelial cells
201 and pericytes (Figure 3C). At 5 dpf, the basement membrane was noticeably lacking gold particles
202 as compared to 3 dpf (Figure 3D), with a reduced average gold intensity of 0.85 ± 0.02 (Figure
203 3G). Like at 3 dpf, the tight junctions remained functional at 5 dpf, based on their capacity to halt
204 gold nanoparticles at the kissing points between neighboring endothelial cells (76/76 functional
205 tight junctions; Figure 3D). However, the levels of vesicles both luminally and abluminally were
206 notably decreased to 0.08 ± 0.01 and 0.07 ± 0.01 vesicles/μm, respectively ($p<0.001$ (luminal)
207 and $p<0.0001$ (abluminal), nested one-way ANOVA; Figure 3H and 3I). At 7 dpf the neurovascular
208 cellular interactions remained constant with endothelial cells in close contact with pericytes and
209 neurons, and with an unfilled basement membrane (average gold intensity of 0.91 ± 0.02; Figure
210 3E and 3G). Importantly, the tight junctions remained functional (51/51 functional tight junctions),
211 and the low vesicular densities observed at 5 dpf remained comparably low at 7 dpf with 0.07 ±
212 0.01 vesicles/μm, both luminally and abluminally (Figure 3F, 3H and 3I). Taken together with the
213 fluorescent tracer data, our data suggests that the zebrafish BBB becomes functional at 5 dpf via
214 suppression of vesicular trafficking.
215

216 *Conserved Role of Mfsd2a in Determining BBB Function*

217 Given the important role of suppressing transcytosis in determining the developmental maturation
218 of the zebrafish BBB, we wondered whether the key mammalian barrier regulator Mfsd2a, which
219 suppresses caveolae mediated transcytosis (Ben-Zvi et al., 2014; Andreone et al., 2017), plays a
220 conserved role in zebrafish. Zebrafish contain two paralogues of *Mfsd2a*, *mfsd2aa* and *mfsd2ab*.
221 *Mfsd2aa* is 61% identical to human *MFSD2A* and 62% identical to mouse *Mfsd2a* (Figure 4 –
222 Supplement 1A). *Mfsd2ab*, on the other hand, is 64% identical to human *MFSD2A* and mouse
223 *Mfsd2a* (Figure 4 – Supplement 1A). The two paralogues are only 68% identical to each other,
224 but they both contain the lipid binding domain that is critical for governing barrier properties (Figure
225 4 – Supplement 1A; Andreone et al., 2017). Given the lack of a clear paralogue that most closely
226 resembles *Mfsd2a*, we generated CRISPR mutants for both paralogues independently.
227 *Mfsd2aa*$^{hm37/hm37}$ mutants have a 7 bp deletion in exon 2 (Figure 4 – Supplement 1B) that is
228 predicted to lead to a premature stop codon at amino acid 82 (Figure 4 – Supplement 1A; black
229 box). Homozygous *mfsd2aa* mutants are viable and fertile. *Mfsd2ab*$^{hm38/hm38}$ mutants have a 19
230 bp deletion in exon 5 (Figure 4 – Supplement 1B) that is predicted to lead to a premature stop
231 codon at amino acid 175 (Figure 4 – Supplement 1A; black box). Homozygous *mfsd2ab* mutants
232 are also viable and fertile. Neither mutant displayed obvious angiogenic defects, similar to the
233 normal vasculature observed in mouse *Mfsd2a* mutants (Ben-Zvi et al., 2014).

234

235 To investigate whether either paralogue was necessary for barrier formation, we performed NHS
236 tracer injection assays as we did to identify the developmental timeline of barrier formation and
237 assayed for midbrain leakage at 5 dpf. In addition to the use of the exogenous injected fluorescent
238 tracer (1 kDa NHS), we also assayed the leakage of the endogenous transgenic serum DBP-
239 EGFP fusion protein (Tg(*l-fabp:DBP-EGFP*)). *Mfsd2aa* mutants displayed about a two-fold
240 increase in midbrain tracer-containing parenchymal cells, both for the injected 1 kDa NHS and
241 the endogenous serum transgene 80 kDa DBP-EGFP, at 5 dpf compared to wildtype sibling

242 controls (Figure 4). These data suggest that mfsd2aa plays a similar role to mouse Mfsd2a in
243 determining barrier properties. Conversely, *mfsd2ab* mutants displayed similarly low levels of
244 tracer-containing parenchymal cells to wildtype controls at 5 dpf in the midbrain (Figure 4 -
245 Supplement 2), indicating that mfsd2ab is dispensable for functional barrier formation. To see if
246 the loss of both paralogues resulted in increased barrier permeability, we investigated
247 *mfsd2aa*$^{hm37/hm37}$*; mfsd2ab*$^{hm38/hm38}$ double mutants for BBB permeability using the endogenous
248 serum DBP-EGFP fusion protein (Figure 4 - Supplement 3). While *mfsd2aa* single mutants
249 displayed the previously observed increase in barrier permeability and *mfsd2ab* single mutants
250 did not, *mfsd2aa*$^{hm37/hm37}$*; mfsd2ab*$^{hm38/hm38}$ double mutants displayed similar levels of increased
251 barrier permeability to the *mfsd2aa* single mutants (Figure 4 - Supplement 3). Taken together,
252 these data suggest that the two paralogues, while structurally similar, play different roles, with
253 zebrafish mfsd2aa and mammalian Mfsd2a sharing a conserved role in determining barrier
254 permeability.
255
256 Given the leakage phenotype in *mfsd2aa* mutants at 5 dpf, we next wanted to examine whether
257 the leakage phenotype persisted into adulthood. To address this, we performed retro-orbital
258 injections of HRP, which has been shown to be confined within the adult zebrafish brain
259 vasculature (Jeong et al., 2008), and allowed the HRP to circulate for 30 minutes. As expected,
260 the wildtype siblings retained the HRP within their blood vessels (Figure 5A). However, *mfsd2aa*
261 mutants exhibited HRP extravasation into the brain parenchyma (Figure 5B), suggesting that the
262 leakage phenotype was not limited to larval fish. Finally, to determine whether this increased
263 permeability was due to increased transcytosis as in *Mfsd2a* knockout mice, we measured
264 vesicular density in capillaries with luminal diameters less than 5 μm from adult mutant and
265 wildtype siblings using TEM. The *mfsd2aa* mutant blood vessels appeared morphologically
266 normal by TEM, composed of a thin single layer of endothelial cells in close contact with pericytes,
267 as observed in their wildtype siblings (Figure 5C and 5D). A closer examination of the endothelial

268 cells revealed electron-dense tight junction complexes between all apposed endothelial cells in
269 both wildtype and *mfsd2aa* mutant fish (Figure 5E and 5F). However, while wildtype fish display
270 similarly low levels of luminal (0.1 vesicles/μm) and abluminal (0.11 vesicles/μm) vesicular
271 densities to those observed at 7 dpf (Figure 5E- 5H), *mfsd2aa* mutant fish display a significant
272 increase in luminal and abluminal vesicular densities (0.29 and 0.27 vesicles/μm, respectively)
273 compared to wildtype siblings (Figure 5E-5H). Interestingly this increase in vesicular abundance
274 is even higher than that observed during early barrier development at 3 dpf (Figure 2). These data
275 also suggest that the increased tracer leakage observed in *mfsd2aa* mutants results from an
276 increase in vesicular trafficking across the BBB, further supporting a conserved role for mfsd2aa
277 in determining barrier properties. In contrast to *mfsd2aa* mutants, *mfsd2ab* mutants displayed
278 similar levels of abluminal and luminal vesicular pit density to wildtype siblings (Figure 5 -
279 Supplement 1), further demonstrating that the paralog *mfsd2ab* does not play a conserved role in
280 determining barrier properties in zebrafish.
281
282 **Discussion**
283 One of the major advantages to studying the BBB in zebrafish is the ability to perform live imaging
284 of tracer permeability dynamics. We provide some of the first data on the dynamics of immature
285 barrier leakage. At 3 dpf, we observed two types of leakage, the gradual overall increase in the
286 parenchyma and rare transient bursts, both from a migrating sprout and established blood
287 vessels. We attribute the gradual diffuse increase in parenchymal tracer uptake to the high levels
288 of vesicular trafficking observed in our TEM analyses in which the endothelial basement
289 membrane became filled with gold nanoparticles. Therefore, the parenchymal Dextran intensity
290 measurements provide a direct proxy for the rates of BBB transcytosis *in vivo*. The rarer bursts of
291 leakage, on the other hand, could be due to fleeting tight junctional ruptures between neighboring
292 endothelial cells rather than increased vesicular trafficking. As these events were extremely
293 scarce during our time lapse imaging, it would be nearly impossible to capture these potential

294 junctional breaches by TEM to confirm this hypothesis. However, with continuing advances in the
295 resolution of fluorescence microscopy, we could use zebrafish to resolve whether these two types
296 of leakage, gradual and bursting, proceed through the same or different subcellular routes into
297 the brain parenchyma, either paracellularly or transcellularly.
298
299 Among the various clathrin-independent transcytotic pathways (Tuma and Hubbard, 2003;
300 Sandvig et al., 2018), caveolae are particularly abundant in vascular endothelial cells (Frank et
301 al., 2003). Caveolae are caveolin-coated 50-100 nm flask-shaped invaginations of the plasma
302 membrane (Palade, 1953; Palade, 1961). Furthermore, the suppression of caveolae-mediated
303 transcytosis regulates the development and function of both the mouse blood-retinal barrier and
304 the BBB (Andreone et al., 2017; Chow and Gu, 2017). Taken together, this suggests that the
305 increased transcytosis during early larval stages is most likely caveolae mediated. Interestingly,
306 the linear profile of Dextran uptake in the midbrain at 3 dpf closely resembles the caveolae-
307 mediated uptake of a fluorescently-conjugated aminopeptidase P (APP) antibody in the mouse
308 lung (Oh et al., 2007). While similarly linear, the scale is on the order of minutes in the larval
309 zebrafish brain versus seconds in the mouse lung. This discrepancy in timing is most likely due
310 to the large difference in the vesicular densities between the immature BBB endothelium (average
311 of 2 vesicles/μm^2) and the continuous endothelium of peripheral tissues, which ranges from 30 to
312 98 vesicles/μm^2 on the luminal membrane of diaphragm and myocardial endothelium (Simionescu
313 et al., 1974). Since loss of caveolin 1 is sufficient to precociously seal the blood-retinal barrier at
314 the angiogenic front (Chow and Gu, 2017), it would be interesting in future work to examine
315 whether zebrafish caveolin 1 mutants (Cao et al., 2016), which are viable as homozygotes, also
316 exhibit an earlier onset of BBB maturation.
317
318 BBB permeability is tightly regulated by endothelial cell interactions with pericytes and astroglial
319 cells. For the first time, we visualized their locations under TEM in zebrafish throughout barrier

320 development. Pericytes have been shown to be essential for establishing the mammalian BBB
321 (Armulik et al., 2010; Bell et al., 2010; Daneman et al., 2010). Similarly, pericyte deficient
322 notch3^{fh332} fish display increased BBB permeability in a tight junction independent manner like
323 pericyte-deficient mice (Wang et al., 2014). Our TEM data show that zebrafish pericytes are in
324 close contact with brain endothelial cells (Figures 2 and 5), even at the earliest stage examined
325 (3 dpf; Figure 2), and are embedded within the endothelial basement membrane as in mammals.
326 Our subcellular localization data is in line with a growing body of evidence for the conserved role
327 of pericytes in the zebrafish BBB (Wang et al., 2014; Lei et al., 2017). While zebrafish lack stellate
328 astrocytes, they possess radial glia that express several astrocytic markers, such as Gfap,
329 glutamine synthetase (GS), and Aqp4 (Jeong et al., 2008; Grupp et al., 2010). Previous studies
330 have disagreed on the extent of radial glia interactions with BBB endothelial cells in zebrafish.
331 Some studies report glia-BBB interactions that are similar to those observed in mammals (Jeong
332 et al., 2008), while others report little to no interaction (Grupp et al., 2010). Our TEM data in adult
333 zebrafish do not find a necessity for glial interactions with the brain vasculature, with endothelial
334 cells occasionally in contact with electron-light glia (Figure 5B), but often not (Figure 5A). This
335 appears to be a unique feature of the zebrafish BBB and should be considered carefully when
336 using zebrafish as a model system for the BBB.
337
338 Taken together this study provides a thorough characterization of the development of the
339 zebrafish BBB, highlighting regional differences in timing of maturation and capturing the
340 dynamics of the immature BBB. Furthermore, our developmental TEM series provides the first
341 direct evidence of vesicular trafficking regulating zebrafish BBB development. Finally, we have
342 shown that this down-regulation of vesicular trafficking is necessary for BBB formation, as
343 *mfsd2aa* mutants display increased barrier permeability due to unsuppressed transcytosis. We
344 hope that this work will serve as a launching pad for future studies using zebrafish to understand
345 the molecular regulators of BBB development and homeostasis in vertebrates.

346 **Author Contributions**

347 N.M.O., S.G.M. and C.G. conceived the project and designed experiments. N.M.O. performed all
348 experiments and analyzed all data. N.M.O., S.G.M. and C.G wrote the manuscript.

349

350 **Acknowledgments**

351 We thank members of the Gu and Megason laboratories for data discussion and comments on
352 the manuscript; Dr. Zach O'Brown for discussions and comments on the manuscript; Dr. Bela
353 Anand-Apte (Cleveland Clinic) for providing the transgenic *l-fabp:DBP-EGFP* fish line (Xie et al.,
354 2010) and Dr. Leonard Zon for providing the transgenic Tg(*kdrl:HRAS-mCherry*) line; and the
355 HMS Electron Microscopy Core Facility, with special thanks to Louise Trakimas for all of her
356 assistance in troubleshooting and preparing the TEM samples. This work was supported by the
357 Damon Runyon Cancer Foundation (N.M.O.), the Mahoney postdoctoral fellowship (N.M.O.), the
358 Fidelity Biosciences Research Initiative (C.G.), and the NIH DP1 NS092473 Pioneer Award
359 (C.G.). The research of C.G. was also supported in part by a Faculty Scholar grant from the
360 Howard Hughes Medical Institute.

361 **Materials and Methods**

362

363 **Zebrafish Strains and Maintenance**

364 Zebrafish were maintained at 28.5°C following standard protocols (Westerfield, 1993). All
365 zebrafish work was approved by the Harvard Medical Area Standing Committee on Animals under
366 protocol number 04487. Adult fish were maintained on a standard light-dark cycle from 9 am to
367 11 pm. Adult fish, age 3 months to 2 years, were crossed to produce embryos and larvae. These
368 studies used the AB wildtype strain and the transgenic strains Tg(*l-fabp:DBP-EGFP),*
369 Tg(*kdrl:mCherry*), and Tg(*kdrl:HRAS-mCherry*).

370

371 **Tracer Injections**

372 Larvae were immobilized with tricaine and placed in an agarose injection mold with their hearts
373 facing upwards. 2.3 nl of Alexa Fluor 405 NHS Ester (Thermo Fisher: A30000) or Alexa Fluor 647
374 10 kDa Dextran (Thermo Fisher:D22914) fluorescently conjugated tracers (10 mg/ml) were
375 injected into the cardiac sac using Nanoject II (Drummond Scientific, Broomall, PA). Embryos
376 were then mounted with 1.5% low gelling agarose (Sigma: A9414) in embryo water on 0.17 mm
377 coverslips and imaged live within 2 hours post injection. For developmental electron microscopy
378 experiments, 2.3 nl of 5 nm NHS-activated gold nanoparticles (Cytodiagnostics: CGN5K-5-1,
379 ~1.1^{14} particles/ml in PBS) were injected into the cardiac sac just as for the fluorescently
380 conjugated tracers. After 5 minutes of circulation, the fish were fixed for electron microscopy.
381 Adults were briefly immobilized with tricaine and retroorbitally injected with 3 µl of HRP (2 mg/ml
382 dissolved in PBS) using a 10 µl Hamilton syringe. After 30 minutes of HRP circulation, the brains
383 were fixed in 4% PFA overnight at 4C. Following fixation the brains were washed three times and
384 sectioned coronally with a vibratome (50 µm). Sections were then stained at room temperature in
385 0.05 M Tris-HCl pH 7.6 buffer containing 0.5 mg/ml 3-39 diaminobenzidine (DAB, Sigma Aldrich)
386 and 0.01% hydrogen peroxide.

387 **Transmission Electron Microscopy (TEM)**

388 Fish were anesthetized with tricaine and initially fixed by immersion in 4% paraformaldehyde
389 (VWR:15713-S) /0.1M sodium-cacodylate (VWR:11653). Following this initial fixation, the larval
390 fish and adults with exposed brains were further fixed for 7-14 days in 2% glutaraldehyde (Electron
391 Microscopy Sciences: 16320)/ 4% paraformaldehyde/ 0.1M sodium-cacodylate at room
392 temperature. Following fixation, larvae or dissected brains were washed overnight in 0.1M
393 sodium-cacodylate. Entire larval heads or coronal vibratome free-floating sections of adult brains
394 (50 μm) were post-fixed in 1% osmium tetroxide and 1.5% potassium ferrocyanide, dehydrated,
395 and embedded in epoxy resin. Ultrathin sections of 80 nm were then cut from the block surface
396 and collected on copper grids. The adult sections were counter-stained with Reynold's lead citrate
397 prior to imaging.

398

399 **CRISPR Mutants**

400 *Mfsd2aa* mutant fish were generated by injection of Cas9 RNA and a single guide RNA (5'-
401 GGTGTGTTTTGCGATCGGAG-3') targeting exon 3 into single-cell fertilized wildtype embryos.
402 *Mfsd2ab* mutant fish were generated by injection of Cas9 protein and a single guide RNA (5'-
403 TGAGAGCAGAGTAGGGCACG-3') targeting exon 5 into single-cell fertilized double transgenic
404 Tg(*l-fabp:DBP-EGFP; kdrl:mCherry)* embryos. F0 injected fish were raised, outcrossed to
405 wildtype fish and screened for potential mutant founders by PCR and sequencing. The stable
406 *mfsd2aa* mutant line was genotyped using 5'-AAATCACCTCTTCCAGTGAGGA-3' and 5'-
407 ATAGTAACAAAACGATGCTGAGCC-3' primers. *Mfsd2ab* mutants were genotyped using 5'-
408 GTCTACTCCATTTGCTGTACTTTGC-3' and 5'-CAGGTCAATCTCAGTGCTGATACAG-3'
409 primers.

410

411 **Imaging**

412 All live imaging of tracer permeability was performed on a Leica SP8 laser scanning confocal
413 microscope. Time lapse imaging was performed on the SP8 using a resonance scanner. A
414 1200EX electron microscope (JOEL) equipped with a 2k CCD digital camera (AMT) was used for
415 all TEM studies. Images were visualized and quantified using ImageJ (NIH) and Adobe
416 Photoshop. Time lapse videos were visualized as 3D reconstructions and cropped to highlight
417 particular blood vessels of interest using Imaris software (Bitplane).

418

419 **Tracer Permeability Quantification**

420 All quantification was performed on blinded image sets. Parenchymal cells containing injected
421 tracers outside of the blood vessels were manually counted throughout z-stacks that spanned the
422 entire larval brain in depth. Z-stacks were collected with 0.59 μm z-steps using a 25x water
423 immersion objective on a Leica SP8 laser scanning confocal microscope. The Dextran intensity
424 was measured in six parenchymal regions of average intensity projections of the time lapse videos
425 and averaged as a single value per fish. These values were normalized to the average
426 fluorescence intensity in the lumen at each time point.

427

428 **TEM Quantification**

429 For all TEM quantifications, vesicular density values were calculated from the number of non-
430 clathrin coated flask-shaped vesicles per μm of endothelial luminal or abluminal membrane for
431 each image collected. Embryonic basement membrane gold intensity was measured in three
432 regions per endothelial cell and normalized to luminal gold intensity values within individual
433 images using ImageJ. All images for analysis were collected at 12000x magnification on the JOEL
434 1200EX electron microscope. 10-15 vessels were quantified for each fish, with each color
435 representing a different fish.

436

437 **Statistical Analysis**

438 All statistical analyses were performed using Prism 8 (GraphPad Software). Two group
439 comparisons were analyzed using an unpaired two-tailed t test. Multiple group comparisons were
440 analyzed with one-way ANOVA, followed by a post hoc Tukey's multiple comparison test. Sample
441 size for all experiments was determined empirically using standards generally employed by the
442 field, and no data was excluded when performing statistical analysis. Standard error of the mean
443 was calculated for all experiments and displayed as errors bars in graphs. Statistical details for
444 specific experiments, including exact n values and what n represents, precision measures,
445 statistical tests used, and definitions of significance can be found in the Figure Legends.

446

447 Ablain, J., Durand, E.M., Yang, S., Zhou, Y., and Zon, L.I. 2015. A CRISPR/Cas9 Vector System
448 for Tissue-Specific Gene Disruption in Zebrafish. Dev. Cell **32**(6): 756–764. Elsevier Inc.
449 doi:10.1016/j.devcel.2015.01.032.
450 Albadri, S., Del Bene, F., and Revenu, C. 2017. Genome editing using CRISPR/Cas9-based
451 knock-in approaches in zebrafish. Methods **121-122**: 77–85. Elsevier Inc.
452 doi:10.1016/j.ymeth.2017.03.005.
453 Andreone, B.J., Chow, B.W., Tata, A., Lacoste, B., Ben-Zvi, A., Bullock, K., Deik, A.A., Ginty,
454 D.D., Clish, C.B., and Gu, C. 2017. Blood-Brain Barrier Permeability Is Regulated by Lipid
455 Transport-Dependent Suppression of Caveolae-Mediated Transcytosis. Neuron **94**(3): 581–
456 594.e5. doi:10.1016/j.neuron.2017.03.043.
457 Andreone, B.J., Lacoste, B., and Gu, C. 2015. Neuronal and Vascular Interactions.
458 http://dx.doi.org.ezp-prod1.hul.harvard.edu/10.1146/annurev-neuro-071714-033835. Annual
459 Reviews. doi:10.1146/annurev-neuro-071714-033835.
460 Armer, H.E.J., Mariggi, G., Png, K.M.Y., Genoud, C., Monteith, A.G., Bushby, A.J., Gerhardt, H.,
461 and Collinson, L.M. 2009. Imaging Transient Blood Vessel Fusion Events in Zebrafish by
462 Correlative Volume Electron Microscopy. PLoS ONE **4**(11): e7716–10.
463 doi:10.1371/journal.pone.0007716.
464 Armulik, A., Genové, G., Mäe, M., Nisancioglu, M.H., Wallgard, E., Niaudet, C., He, L., Norlin, J.,
465 Lindblom, P., Strittmatter, K., Johansson, B.R., and Betsholtz, C. 2010. Pericytes regulate the
466 blood-brain barrier. Nature **468**(7323): 557–561. doi:10.1038/nature09522.
467 Bell, R.D., Winkler, E.A., Sagare, A.P., Singh, I., LaRue, B., Deane, R., and Zlokovic, B.V. 2010b.
468 Pericytes control key neurovascular functions and neuronal phenotype in the adult brain and
469 during brain aging. Neuron **68**(3): 409–427. doi:10.1016/j.neuron.2010.09.043.
470 Ben-Zvi, A., Lacoste, B., Kur, E., Andreone, B.J., Mayshar, Y., Yan, H., and Gu, C. 2014. Mfsd2a
471 is critical for the formation and function of the blood-brain barrier. Nature **509**(7501): 507–
472 511. doi:10.1038/nature13324.
473 Brightman, M.W., and Reese, T.S. 1969. Junctions between intimately apposed cell membranes
474 in the vertebrate brain. J. Cell Biol. **40**(3): 648–677.
475 Campbell, M., Kiang, A.-S., Kenna, P.F., Kerskens, C., Blau, C., O'Dwyer, L., Tivnan, A., Kelly,
476 J.A., Brankin, B., Farrar, G.-J., and Humphries, P. 2008. RNAi-mediated reversible opening
477 of the blood-brain barrier. J. Gene Med. **10**(8): 930–947. doi:10.1002/jgm.1211.
478 Cao, J., Navis, A., Ben D Cox, Dickson, A.L., Gemberling, M., Karra, R., Bagnat, M., and Poss,
479 K.D. 2016. Single epicardial cell transcriptome sequencing identifies Caveolin 1 as an
480 essential factor in zebrafish heart regeneration. Development **143**(2): 232–243. Oxford
481 University Press for The Company of Biologists Limited. doi:10.1242/dev.130534.
482 Chow, B.W., and Gu, C. 2017. Gradual Suppression of Transcytosis Governs Functional Blood-
483 Retinal Barrier Formation. Neuron **93**(6): 1325–1333.e3. Elsevier Inc.
484 doi:10.1016/j.neuron.2017.02.043.
485 Daneman, R., Zhou, L., Kebede, A.A., and Barres, B.A. 2010. Pericytes are required for blood-
486 brain barrier integrity during embryogenesis. Nature **468**(7323): 562–566.
487 doi:10.1038/nature09513.
488 Fleming, A., Diekmann, H., and Goldsmith, P. 2013. Functional characterisation of the maturation
489 of the blood-brain barrier in larval zebrafish. PLoS ONE **8**(10): e77548.
490 doi:10.1371/journal.pone.0077548.
491 Franco, C.A., Jones, M.L., Bernabeu, M.O., Geudens, I., Mathivet, T., Rosa, A., Lopes, F.M.,
492 Lima, A.P., Ragab, A., Collins, R.T., Phng, L.-K., Coveney, P.V., and Gerhardt, H. 2015.
493 Dynamic Endothelial Cell Rearrangements Drive Developmental Vessel Regression. PLoS
494 Biol. **13**(4): e1002125–19. doi:10.1371/journal.pbio.1002125.
495 Frank, P.G., Woodman, S.E., Park, D.S., and Lisanti, M.P. 2003. Caveolin, Caveolae, and
496 Endothelial Cell Function. Arterioscler. Thromb. Vasc. Biol. **23**(7): 1161–1168.
497 doi:10.1161/01.ATV.0000070546.16946.3A.

498 Gagnon, J.A., Valen, E., Thyme, S.B., Huang, P., Ahkmetova, L., Pauli, A., Montague, T.G.,
499 Zimmerman, S., Richter, C., and Schier, A.F. 2014. Efficient Mutagenesis by Cas9 Protein-
500 Mediated Oligonucleotide Insertion and Large-Scale Assessment of Single-Guide RNAs.
501 PLoS ONE **9**(5): e98186–8. doi:10.1371/journal.pone.0098186.
502 Geudens, I., Coxam, B., Alt, S., Gebala, V., Vion, A.-C., Rosa, A., and Gerhardt, H. 2018. Arterio-
503 Venous Remodeling in the Zebrafish Trunk Is Controlled by Genetic Programming and Flow-
504 Mediated Fine-Tuning. : 1–32. doi:10.1101/403550.
505 Geudens, I., Herpers, R., Hermans, K., Segura, I., Ruiz de Almodovar, C., Bussmann, J., De
506 Smet, F., Vandevelde, W., Hogan, B.M., Siekmann, A., Claes, F., Moore, J.C., Pistocchi, A.S.,
507 Loges, S., Mazzone, M., Mariggi, G., Bruyère, F., Cotelli, F., Kerjaschki, D., Noël, A., Foidart,
508 J.-M., Gerhardt, H., Ny, A., Langenberg, T., Lawson, N.D., Duckers, H.J., Schulte-Merker, S.,
509 Carmeliet, P., and Dewerchin, M. 2010. Role of Delta-like-4/Notch in the Formation and
510 Wiring of the Lymphatic Network in Zebrafish. Arterioscler. Thromb. Vasc. Biol. **30**(9): 1695–
511 1702. doi:10.1161/ATVBAHA.110.203034.
512 Grupp, L., Wolburg, H., and Mack, A.F. 2010. Astroglial structures in the zebrafish brain. Journal
513 of Comparative Neurology **518**(21): 4277–4287. Wiley Subscription Services, Inc., A Wiley
514 Company. doi:10.1002/cne.22481.
515 Guemez-Gamboa, A., Nguyen, L.N., Yang, H., Zaki, M.S., Kara, M., Ben-Omran, T., Akizu, N.,
516 Rosti, R.O., Rosti, B., Scott, E., Schroth, J., Copeland, B., Vaux, K.K., Cazenave-Gassiot, A.,
517 Quek, D.Q.Y., Wong, B.H., Tan, B.C., Wenk, M.R., Gunel, M., Gabriel, S., Chi, N.C., Silver,
518 D.L., and Gleeson, J.G. 2015. Inactivating mutations in MFSD2A, required for omega-3 fatty
519 acid transport in brain, cause a lethal microcephaly syndrome. Nat. Genet. **47**(7): 809–813.
520 doi:10.1038/ng.3311.
521 Harel, T., Quek, D.Q.Y., Wong, B.H., Cazenave-Gassiot, A., Wenk, M.R., Fan, H., Berger, I.,
522 Shmueli, D., Shaag, A., Silver, D.L., Elpeleg, O., and Edvardson, S. 2018. Homozygous
523 mutation in MFSD2A, encoding a lysolipid transporter for docosahexanoic acid, is associated
524 with microcephaly and hypomyelination. Neurogenetics **19**(4): 227-235. doi:10.1007/s10048-
525 018-0556-6.
526 Herbert, S.P., Cheung, J.Y.M., and Stainier, D.Y.R. 2012. Determination of Endothelial Stalk
527 versus Tip Cell Potential during Angiogenesis by H2.0-like Homeobox-1. Current Biology
528 **22**(19): 1789–1794. Elsevier Ltd. doi:10.1016/j.cub.2012.07.037.
529 Herbert, S.P., Huisken, J., Kim, T.N., Feldman, M.E., Houseman, B.T., Wang, R.A., Shokat, K.M.,
530 and Stainier, D.Y.R. 2009. Arterial-venous segregation by selective cell sprouting: an
531 alternative mode of blood vessel formation. Science **326**(5950): 294–298.
532 doi:10.1126/science.1178577.
533 Hogan, B.M., and Schulte-Merker, S. 2017. How to Plumb a Pisces: Understanding Vascular
534 Development and Disease Using Zebrafish Embryos. Dev. Cell **42**(6): 567–583. Elsevier.
535 doi:10.1016/j.devcel.2017.08.015.
536 Hwang, W.Y., Fu, Y., Reyon, D., Maeder, M.L., Tsai, S.Q., Sander, J.D., Peterson, R.T., Yeh, J.-
537 R.J., and Joung, J.K. 2013. Efficient genome editing in zebrafish using a CRISPR-Cas
538 system. Nat. Biotechnol. **31**(3): 227–229. doi:10.1038/nbt.2501.
539 Janzer, R.C., and Raff, M.C. 1987. Astrocytes induce blood-brain barrier properties in endothelial
540 cells. Nature **325**(6101): 253–257. doi:10.1038/325253a0.
541 Jin, S.-W., Beis, D., Mitchell, T., Chen, J.-N., and Stainier, D.Y.R. 2005. Cellular and molecular
542 analyses of vascular tube and lumen formation in zebrafish. Development **132**(23): 5199–
543 5209. The Company of Biologists Ltd. doi:10.1242/dev.02087.
544 Jeong, J.-Y., Kwon, H.-B., Ahn, J.-C., Kang, D., Kwon, S.-H., Park, J.A., and Kim, K.-W. 2008.
545 Functional and developmental analysis of the blood–brain barrier in zebrafish. Brain Res.
546 Bull. **75**(5): 619–628. doi:10.1016/j.brainresbull.2007.10.043.

547 Lei, D., Jin, X., Wen, L., Dai, H., Ye, Z., and Wang, G. 2017. bmp3 is Required for Integrity of
548 Blood Brain Barrier by Promoting Pericyte Coverage in Zebrafish Embryos. *Current Molecular*
549 *Medicine*, *17*(4).
550 Matsuoka, R.L., Marass, M., Avdesh, A., Helker, C.S., Maischein, H.-M., Grosse, A.S., Kaur, H.,
551 Lawson, N.D., Herzog, W., and Stainier, D.Y. 2016. Radial glia regulate vascular patterning
552 around the developing spinal cord. Elife **5**: 1328. doi:10.7554/eLife.20253.
553 Nitta, T., Hata, M., Gotoh, S., Seo, Y., Sasaki, H., Hashimoto, N., Furuse, M., and Tsukita, S.
554 2003. Size-selective loosening of the blood-brain barrier in claudin-5-deficient mice. J. Cell
555 Biol. **161**(3): 653–660. Rockefeller University Press. doi:10.1083/jcb.200302070.
556 O'Brown, N.M., Pfau, S.J., and Gu, C. 2018. Bridging barriers: a comparative look at the blood–
557 brain barrier across organisms. **32**(7-8): 466–478. doi:10.1101/gad.309823.117.
558 Oh, P., Borgström, P., Witkiewicz, H., Li, Y., Borgström, B.J., Chrastina, A., Iwata, K., Zinn, K.R.,
559 Baldwin, R., Testa, J.E., and Schnitzer, J.E. 2007. Live dynamic imaging of caveolae pumping
560 targeted antibody rapidly and specifically across endothelium in the lung. Nat. Biotechnol.
561 **25**(3): 327–337. doi:10.1038/nbt1292.
562 Palade, G.E. 1953. Fine structure of blood capillaries. J. Appl. Phys. **24**: 1424.
563 Palade, G.E. 1961. Blood capillaries of the heart and other organs. Circulation **24**: 368–388.
564 Phng, L.-K., Potente, M., Leslie, J.D., Babbage, J., Nyqvist, D., Lobov, I., Ondr, J.K., Rao, S.,
565 Lang, R.A., Thurston, G., and Gerhardt, H. 2009. Nrarp Coordinates Endothelial Notch and
566 Wnt Signaling to Control Vessel Density in Angiogenesis. Dev. Cell **16**(1): 70–82. Elsevier.
567 doi:10.1016/j.devcel.2008.12.009.
568 Quiñonez-Silvero, C., Hübner, K., and Herzog, W. 2019. Development of the brain vasculature
569 and the blood-brain barrier in zebrafish. Dev. Biol.: 1–34. Elsevier Inc.
570 doi:10.1016/j.ydbio.2019.03.005.
571 Reese, T.S., and Karnovsky, M.J. 1967. Fine structural localization of a blood-brain barrier to
572 exogenous peroxidase. J. Cell Biol. **34**(1): 207–217. The Rockefeller University Press.
573 Sanchez-Covarrubias, L., Slosky, L.M., Thompson, B.J., Davis, T.P., and Ronaldson, P.T. 2014.
574 Transporters at CNS barrier sites: obstacles or opportunities for drug delivery? Curr. Pharm.
575 Des. **20**(10): 1422–1449.
576 Sandvig, K., Kavaliauskiene, S., and Skotland, T. 2018. Clathrin-independent endocytosis: an
577 increasing degree of complexity. Histochem. Cell Biol. **150**(2): 107–118. doi:10.1007/s00418-
578 018-1678-5.
579 Santoro, M.M., Samuel, T., Mitchell, T., Reed, J.C., and Stainier, D.Y.R. 2007. Birc2 (cIap1)
580 regulates endothelial cell integrity and blood vessel homeostasis. Nat. Genet. **39**(11): 1397–
581 1402. doi:10.1038/ng.2007.8.
582 Simionescu, M., Simionescu, N., and Palade, G.E. 1974. Morphometric data on the endothelium
583 of blood capillaries. J. Cell Biol. **60**(1): 128–152. Rockefeller University Press.
584 doi:10.1083/jcb.60.1.128.
585 Sohet, F., Lin, C., Munji, R.N., Lee, S.Y., Ruderisch, N., Soung, A., Arnold, T.D., Derugin, N.,
586 Vexler, Z.S., Yen, F.T., and Daneman, R. 2015. LSR/angulin-1 is a tricellular tight junction
587 protein involved in blood-brain barrier formation. J. Cell Biol. **208**(6): 703–711. Rockefeller
588 University Press. doi:10.1083/jcb.201410131.
589 Stewart, P.A., and Wiley, M.J. 1981. Developing nervous tissue induces formation of blood-brain
590 barrier characteristics in invading endothelial cells: a study using quail--chick transplantation
591 chimeras. Dev. Biol. **84**(1): 183–192.
592 Tuma, P.L., and Hubbard, A.L. 2003. Transcytosis: Crossing Cellular Barriers. Physiological
593 Reviews **83**(3): 871–932. doi:10.1152/physrev.00001.2003.
594 Umans, R.A., Henson, H.E., Mu, F., Parupalli, C., Ju, B., Peters, J.L., Lanham, K.A., Plavicki,
595 J.S., and Taylor, M.R. 2017. CNS angiogenesis and barriergenesis occur simultaneously.
596 Dev. Biol. **425**(2): 101–108. doi:10.1016/j.ydbio.2017.03.017.

597 Vanhollebeke, B., Stone, O.A., Bostaille, N., Cho, C., Zhou, Y., Maquet, E., Gauquier, A.,
598 Cabochette, P., Fukuhara, S., Mochizuki, N., Nathans, J., and Stainier, D.Y. 2015. Tip cell-
599 specific requirement for an atypical Gpr124- and Reck-dependent Wnt/β-catenin pathway
600 during brain angiogenesis. Elife **4**. doi:10.7554/eLife.06489.
601 Varshney, G.K., Sood, R., and Burgess, S.M. 2015. Understanding and Editing the Zebrafish
602 Genome. *In* Advances in Genetics. Elsevier Ltd. doi:10.1016/bs.adgen.2015.09.002.
603 Wang, Y., Pan, L., Moens, C.B., and Appel, B. 2014. Notch3 establishes brain vascular integrity
604 by regulating pericyte number. Development **141**(2): 307–317. Oxford University Press for
605 The Company of Biologists Limited. doi:10.1242/dev.096107.
606 Westerfield, M. 1993. The zebrafish book: a guide for the laboratory use of zebrafish (Brachydanio
607 rerio).
608 Wilkinson, R.N., and van Eeden, F.J.M. 2014. The Zebrafish as a Model of Vascular Development
609 and Disease. *In* Genetics of Cardiovascular Disease, 1st edition. Elsevier Inc.
610 doi:10.1016/B978-0-12-386930-2.00005-7.
611 Xie, J., Farage, E., Sugimoto, M., and Anand-Apte, B. 2010. A novel transgenic zebrafish model
612 for blood-brain and blood-retinal barrier development. BMC Dev. Biol. **10**: 76.
613 doi:10.1186/1471-213X-10-76.
614 Yanagida, K., Liu, C.H., Faraco, G., Galvani, S., Smith, H.K., Burg, N., Anrather, J., Sanchez, T.,
615 Iadecola, C., and Hla, T. 2017. Size-selective opening of the blood–brain barrier by targeting
616 endothelial sphingosine 1–phosphate receptor 1. Proc. Natl. Acad. Sci. U.S.A. **114**(17):
617 4531–4536. doi:10.1073/pnas.1618659114.
618 Zhao, Z., Nelson, A.R., Betsholtz, C., and Zlokovic, B.V. 2015. Establishment and Dysfunction of
619 the Blood-Brain Barrier. Cell **163**(5): 1064–1078. doi:10.1016/j.cell.2015.10.067.

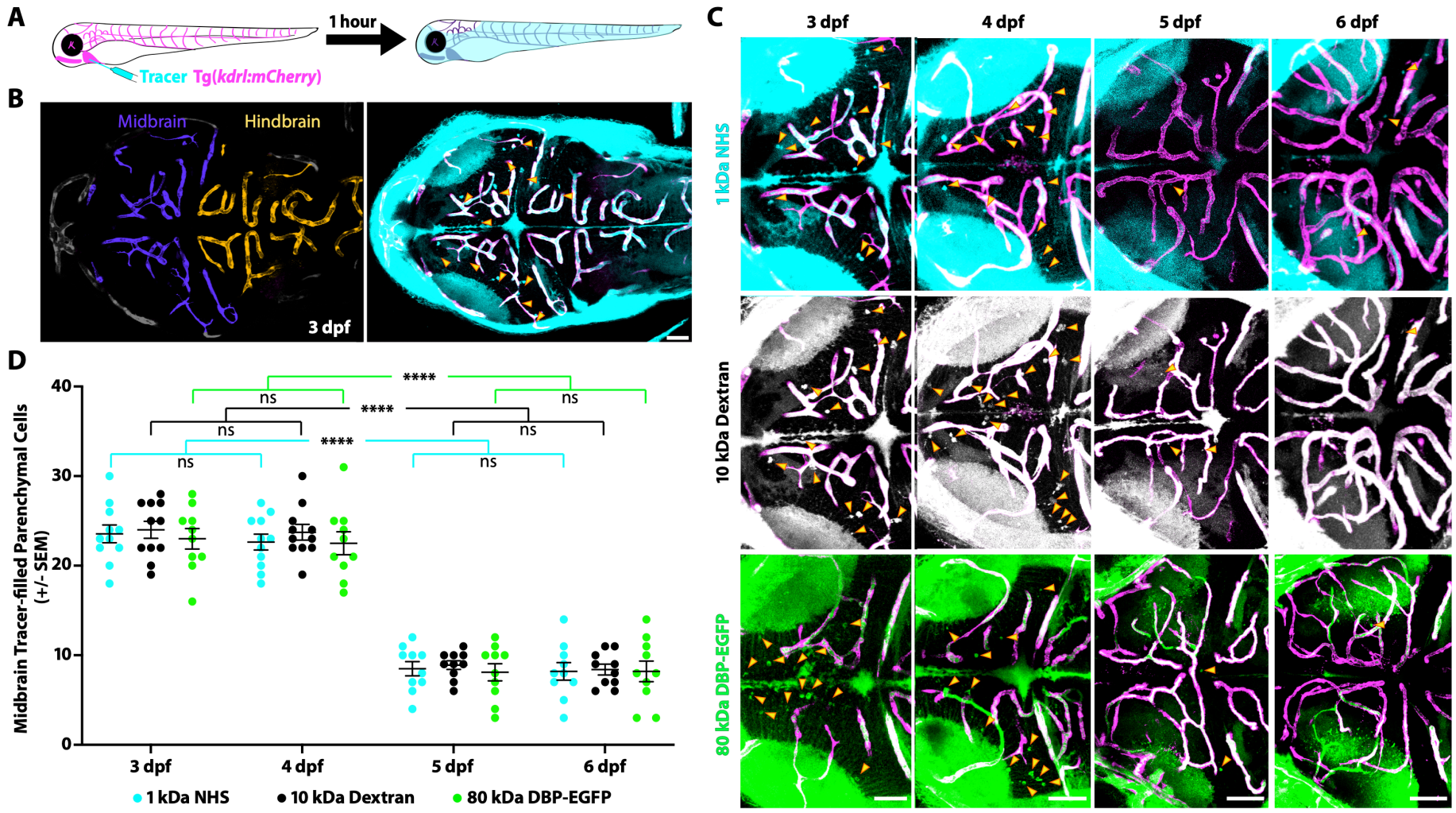
A
1 hour
Tracer
Tg(kdrl:mCherry)
B
Midbrain
Hindbrain
3 dpf
C
3 dpf
4 dpf
5 dpf
6 dpf
1 kDa NHS
10 kDa Dextran
80 kDa DBP-EGFP
D
Midbrain Tracer-filled Parenchymal Cells (+/- SEM)
40
30
20
10
0
****
ns
3 dpf
4 dpf
5 dpf
6 dpf
1 kDa NHS
10 kDa Dextran
80 kDa DBP-EGFP

621 **Figure 1. The midbrain BBB becomes functional at 5 dpf.** (A) Diagram of the tracer leakage
622 assay. Fluorescently conjugated tracers (turquoise) were injected intracardially into transgenic
623 fish that express mCherry in the vasculature (magenta; Tg(*kdrl:mCherry*)) and allowed to circulate
624 for one hour before imaging. (B) Dorsal view maximum intensity projection of the larval brain
625 vasculature at 3 dpf. Left image is pseudo-colored to demarcate the midbrain (violet) and the
626 hindbrain (gold) vasculature. Right image shows the NHS tracer (turquoise) in the entire larval
627 brain, with a large number of tracer-filled parenchymal cells marked by yellow arrowheads in the
628 midbrain. (C) Representative dorsal view maximum intensity projections of larval zebrafish
629 midbrains at different developmental stages reveal increased permeability at 3 and 4 dpf
630 compared to 5 and 6 dpf. The increased early permeability was observed with two injected tracers
631 of different sizes, a 1 kDa NHS (turquoise) and a 10 kDa Dextran (white), as well with an 80 kDa
632 transgenic serum protein DBP-EGFP (green). Yellow arrowheads demarcate the tracer-filled
633 parenchymal cells outside of the vasculature (magenta). Scale bars represent 50 μm. (D)
634 Quantification of tracer-filled parenchymal cells in the midbrain between 3 and 6 dpf reveals a
635 significant decrease in tracer uptake at 5 dpf. There was no difference in the number of
636 parenchymal cells that picked up the different tracers at any time point. There was no significant
637 change from 3 to 4 dpf or from 5 to 6 dpf, suggesting that the barrier seals around 5 dpf. N = 10-
638 11 fish, each represented as a single dot on the plot. The mean and the standard error are drawn
639 in black for each tracer and stage. **** $p<0.0001$, ns is not significant.

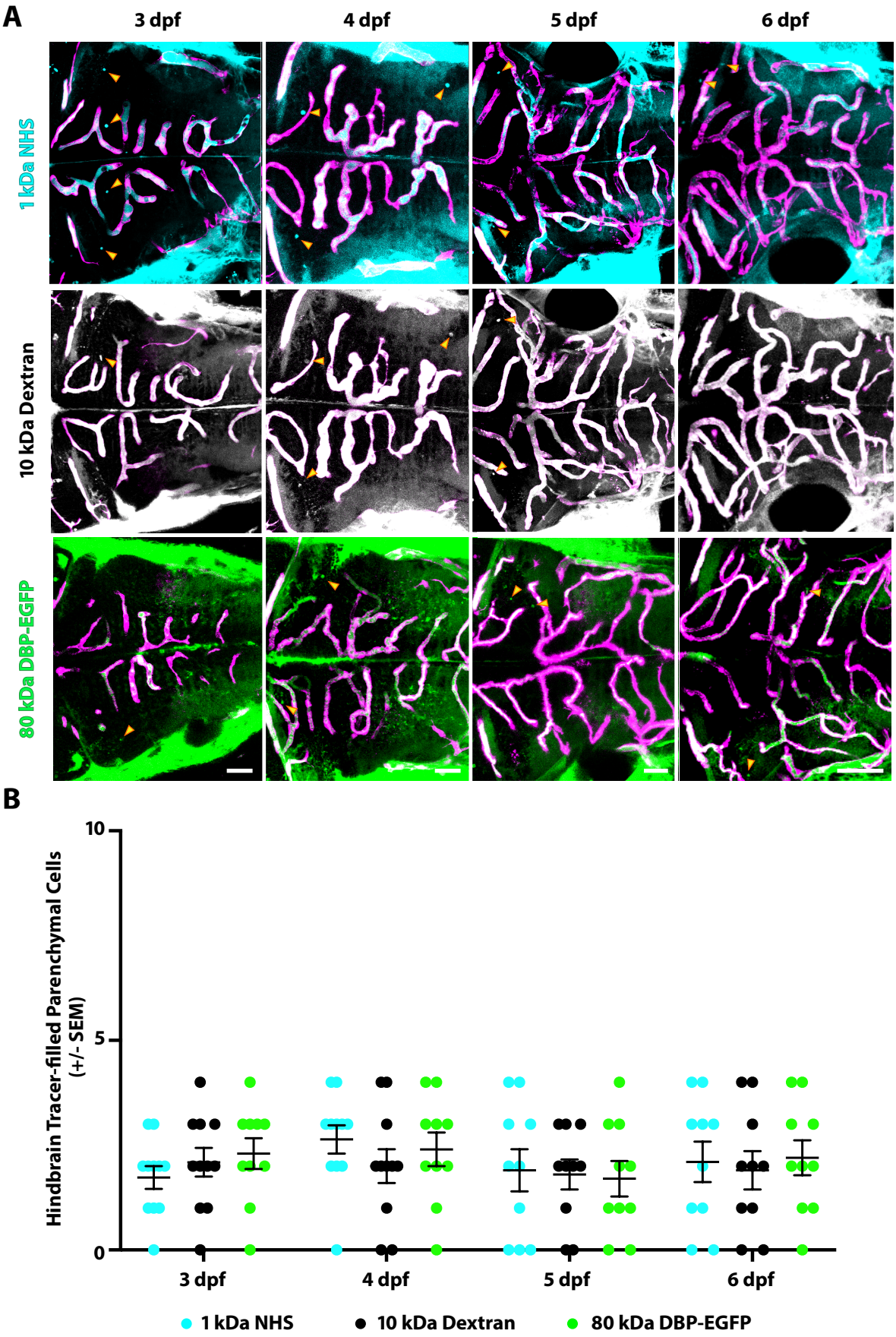
A
3 dpf
4 dpf
5 dpf
6 dpf
1 kDa NHS
10 kDa Dextran
80 kDa DBP-EGFP
B
Hindbrain Tracer-filled Parenchymal Cells
(+/- SEM)
10
5
0
3 dpf
4 dpf
5 dpf
6 dpf
1 kDa NHS
10 kDa Dextran
80 kDa DBP-EGFP

640

641 **Figure 1 – Supplement 1. The hindbrain has a functional BBB at 3 dpf.** (A) Representative
642 dorsal view maximum intensity projections of larval zebrafish hindbrains at different
643 developmental stages reveals low permeability at 3 dpf that stays constant until 6 dpf. This low
644 permeability was observed with two injected tracers of different sizes, a 1 kDa NHS (turquoise)
645 and a 10 kDa Dextran (white), as well with an 80 kDa transgenic serum protein DBP-EGFP
646 (green). Yellow arrowheads demarcate the few tracer-filled parenchymal cells outside of the
647 vasculature (magenta). Scale bars represent 50 μm. (B) Quantification of tracer-filled
648 parenchymal cells in the hindbrain between 3 and 6 dpf reveals low tracer uptake beginning at 3
649 dpf. There was no difference in the number of parenchymal cells that picked up the different
650 tracers at any time point. N = 10-11 fish, each represented as a single dot on the plot. The mean
651 and the standard error are drawn in black for each tracer and stage.

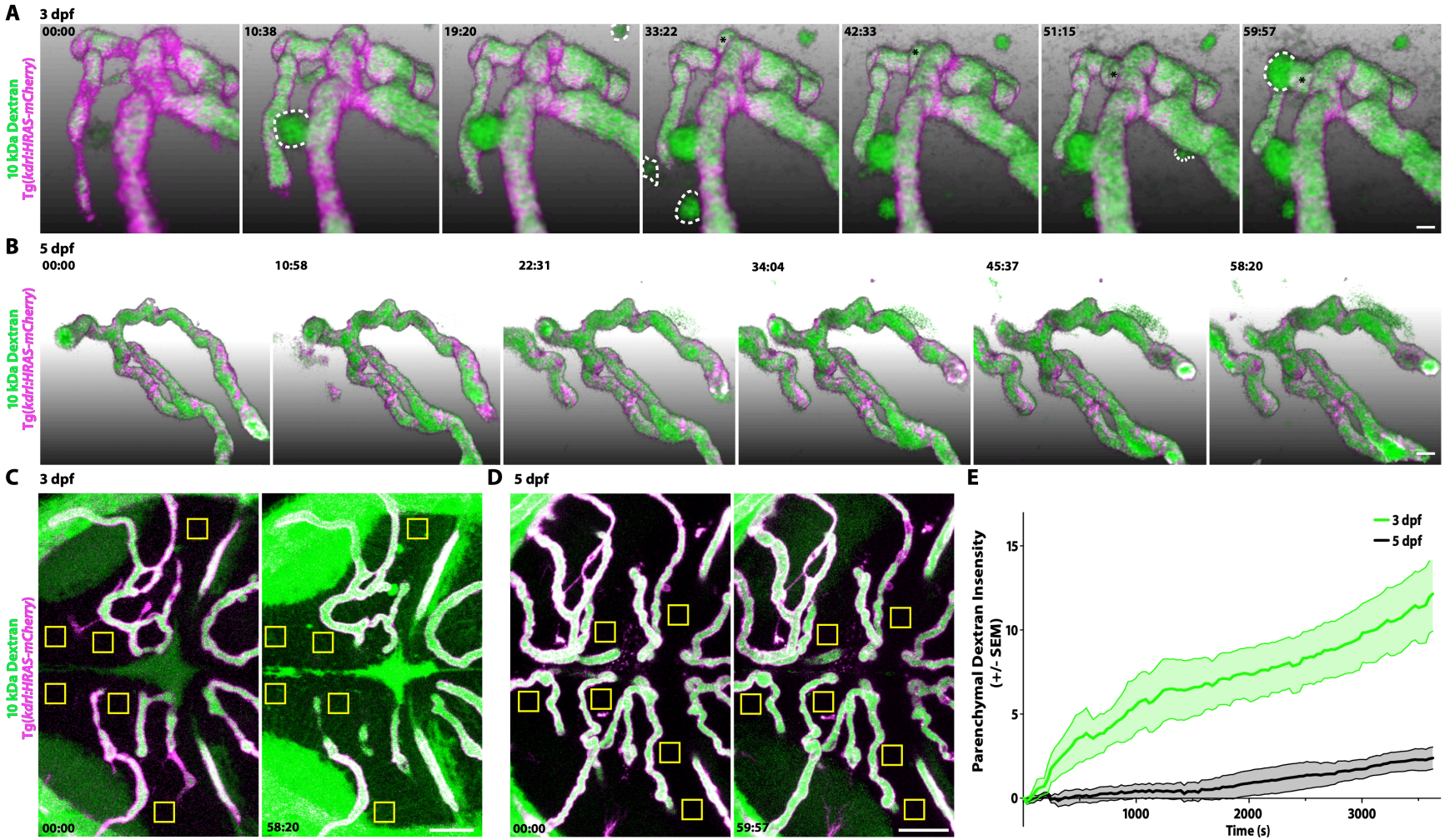
A
3 dpf
00:00
10:38
19:20
33:22
42:33
51:15
59:57
10 kDa Dextran
Tg(kdrl:HRAS-mCherry)
B
5 dpf
00:00
10:58
22:31
34:04
45:37
58:20
10 kDa Dextran
Tg(kdrl:HRAS-mCherry)
C
3 dpf
10 kDa Dextran
Tg(kdrl:HRAS-mCherry)
00:00
58:20
D
5 dpf
00:00
59:57
E
3 dpf
5 dpf
Parenchymal Dextran Insensity
(+/- SEM)
15
10
5
0
1000
2000
3000
Time (s)

653 **Figure 2. Dynamic tracer leakage in the developing BBB via live imaging.** (A) Time course
654 stills from Video 1 of tracer leakage at 3 dpf reveal an increase in parenchymal cells absorbing
655 the Dextran tracer (outlined by dashed white lines) as well as a general increase in overall Dextran
656 (green) intensity outside of the vasculature (magenta). An angiogenic tip cell becomes apparent
657 at 33:23 and is demarcated by an asterisk (*). This tip cell produces two separate bursts of
658 leakage observed in Video 2. (B) Time course stills of Dextran tracer dynamics at 5 dpf reveals a
659 mature BBB, with reduced overall Dextran extravasation into the brain parenchyma. The scale
660 bars represent 10 μm. (C and D) Dorsal maximum intensity projection of the midbrain at 3 dpf (C)
661 and 5 dpf (D) at the first and last time point examined. While there is a large increase in overall
662 parenchymal Dextran intensity over time at 3 dpf, the 5 dpf midbrain parenchyma appears
663 relatively unaltered after an hour of Dextran circulation. Boxed regions are representative of the
664 six areas per fish used for analysis in E. The scale bars represent 50 μm. (E) Quantification of
665 Dextran intensity in the brain parenchyma over time at 3 dpf (green) and 5 dpf (black) shows a
666 significant difference in tracer leakage dynamics ($p<0.0001$, Mann Whitney test), with both more
667 total Dextran accumulation and a faster rate of Dextran accumulation in the brain parenchyma at
668 3 dpf. N=6 fish.

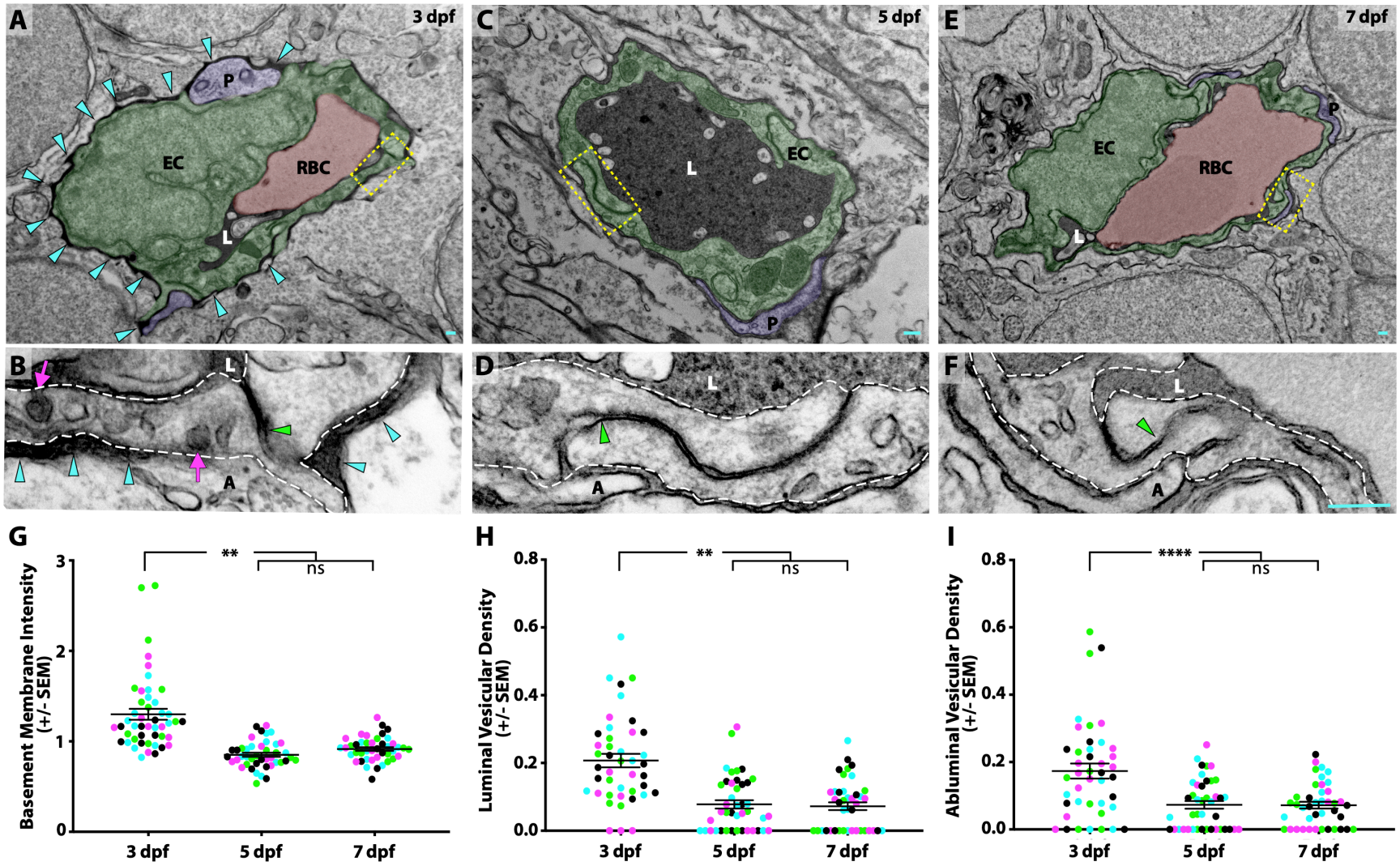
A
3 dpf
P
EC
RBC
L
B
L
A
C
5 dpf
L
EC
P
D
L
A
E
7 dpf
P
EC
RBC
L
F
L
A
G
Basement Membrane Intensity (+/- SEM)
**
ns
3 dpf
5 dpf
7 dpf
H
Luminal Vesicular Density (+/- SEM)
**
ns
3 dpf
5 dpf
7 dpf
I
Abluminal Vesicular Density (+/- SEM)
****
ns
3 dpf
5 dpf
7 dpf

670 **Figure 3. Suppression of transcytosis determines the timing of functional BBB formation.**
671 (A, C, E) TEM images of individual blood vessel cross-sections after injection of electron-dense
672 gold nanoparticles at 3 dpf (A), 5 dpf (C), and 7 dpf (E). Endothelial cells (EC) are pseudo-colored
673 green, pericytes (P) are pseudo-colored purple and red blood cells (RBC) are pseudo-colored red
674 when present in the lumen (L). Turquoise arrowheads highlight the gold-filled basement
675 membrane at 3 dpf (A). (B, D, F) High magnification images (25000x) of the areas boxed in A, C,
676 and E, respectively, with the endothelial cells outlined with white dashed lines. The images are
677 oriented with the lumen (L) on top and the ablumen (A) on the bottom. Tight junctions are
678 functional as early as 3 dpf (B), as seen by their ability to halt the gold nanoparticles at the so-
679 called "kissing point" (green arrowhead), and remain functional throughout development (D and
680 F). Even though the tight junctions are functional at 3 dpf, the endothelial basement membrane is
681 filled with electron-dense gold nanoparticles (B, turquoise arrowheads). This appears to be due
682 to an elevated level of luminal and abluminal gold-filled vesicles (magenta arrows). The scale bars
683 represent 200 nm. (G) Quantification of the endothelial basement membrane gold intensity
684 normalized to luminal gold intensity. (H and I) Quantification of the vesicular densities both on
685 the luminal (H) and abluminal (I) membrane of endothelial cells reveals a suppression of vesicular
686 densities beginning at 5 dpf that remains constant at 7 dpf. N=4 fish, each marked with a different
687 color, with at least 10 blood vessels quantified for each fish. **** $p<0.0001$, ** $p<0.01$, ns is not
688 significant.

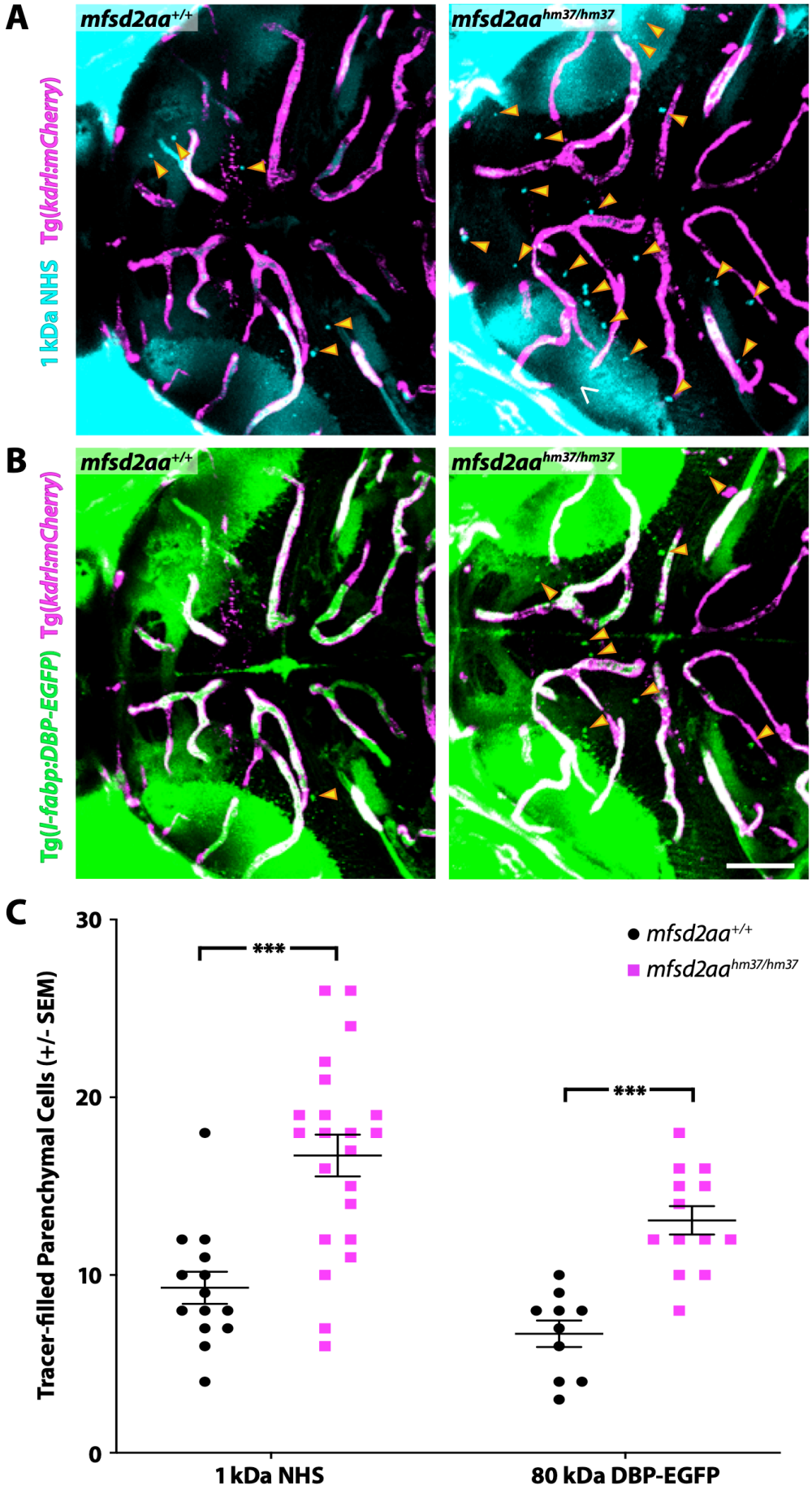
A
mfsd2aa+/+
mfsd2aahm37/hm37
1 kDa NHS Tg(kdrl:mCherry)
B
mfsd2aa+/+
mfsd2aahm37/hm37
Tg(l-fabp:DBP-EGFP) Tg(kdrl:mCherry)
C
Tracer-filled Parenchymal Cells (+/- SEM)
30
20
10
0
***
***
mfsd2aa+/+
mfsd2aahm37/hm37
1 kDa NHS
80 kDa DBP-EGFP

689

690 **Figure 4. *Mfsd2aa* mutants exhibit increased BBB permeability.** (A) Representative maximum
691 intensity projection images of the midbrain of wildtype and *mfsd2aa* mutants injected with a
692 fluorescent 1 kDa NHS tracer (turquoise) at 5 dpf. *Mfsd2aa* mutants have an increased number
693 of NHS-filled parenchymal cells (yellow arrowheads) that lie outside of the vasculature (magenta;
694 Tg(*kdrl:mCherry*)). (B) Representative maximum intensity projection images of the midbrain of
695 wildtype and *mfsd2aa* mutants expressing the fluorescently labelled 80 kDa transgenic serum
696 protein DBP-EGFP (green) at 5 dpf. *Mfsd2aa* mutants have an increased number of DBP-EGFP-
697 filled parenchymal cells (yellow arrowheads) compared to wildtype siblings. The scale bar
698 represents 50 µm. (C) Quantification of tracer-filled (NHS and DBP-EGFP) parenchymal cells in
699 the midbrain of wildtype (black) and *mfsd2aa* mutants (magenta). *Mfsd2aa* mutants have a
700 significantly increased number of tracer-filled parenchymal cells, both for the injected NHS (A)
701 and the endogenous transgene DBP-EGFP (B). Each individual fish measured is displayed as a
702 single point. The mean and the standard error are drawn as black lines. *** $p < 0.001$, ** $p < 0.01$.

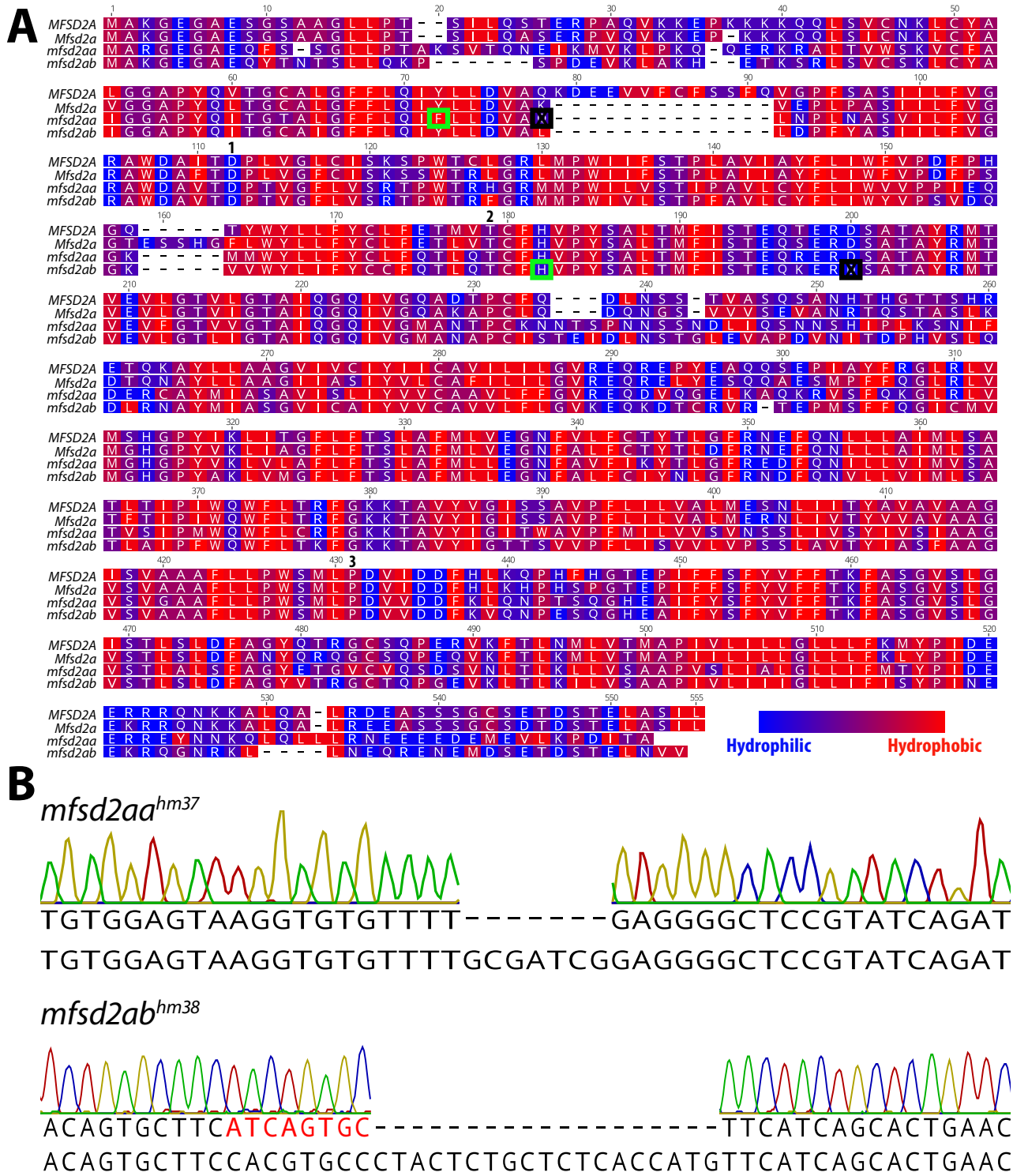
A
MFSD2A
Mfsd2a
mfsd2aa
mfsd2ab
Hydrophilic
Hydrophobic
B
mfsd2aa hm37
TGTGGAGTAAGGTGTGTTTT-------GAGGGGCTCCGTATCAGAT
TGTGGAGTAAGGTGTGTTTTGCGATCGGAGGGGCTCCGTATCAGAT
mfsd2ab hm38
ACAGTGCTTCATCAGTGC----------TTCATCAGCACTGAAC
ACAGTGCTTCCACGTGCCCTACTCTGCTCTCACCATGTTCATCAGCACTGAAC

703

704 **Figure 4 - Supplement 1. Zebrafish have 2 *Mfsd2a* paralogues, *mfsd2aa* and *mfsd2ab*.** (A)
705 Protein alignment of human MFSD2A, mouse Mfsd2a, zebrafish mfsd2aa, and zebrafish mfsd2ab
706 illustrated with a hydrophobicity scale. Red amino acids are hydrophobic and blue amino acids
707 are hydrophilic. Both zebrafish paralogues are highly similar to the human and mouse proteins.
708 Green boxes highlight the genetic lesions in (B) and the black boxes mark the predicted premature
709 stop codons caused by these mutations in *mfsd2aa*$^{hm37/hm37}$ and *mfsd2ab*$^{hm38/hm38}$ mutants.
710 Numbers mark amino acid residues with mutations that have been shown to impact Mfsd2a
711 function:1. Andreone et al., 2017, 2. Guemez-Gamboa et al., 2015, 3. Harel et al., 2018. (B)
712 Sanger sequencing of the *mfsd2aa*^{hm37} and *mfsd2ab*^{hm38} mutations. *Mfsd2aa*$^{hm37/37}$ mutants have
713 a 7 base pair deletion in exon 2 that is predicted to lead to a premature stop codon at amino acid
714 82 (A; black box). *Mfsd2ab*$^{hm38/hm38}$ mutants have an 8 base pair insertion (red letters) and a 19
715 base pair deletion in exon 5 that is predicted to lead to a premature stop codon at amino acid 175
716 (A; black box).

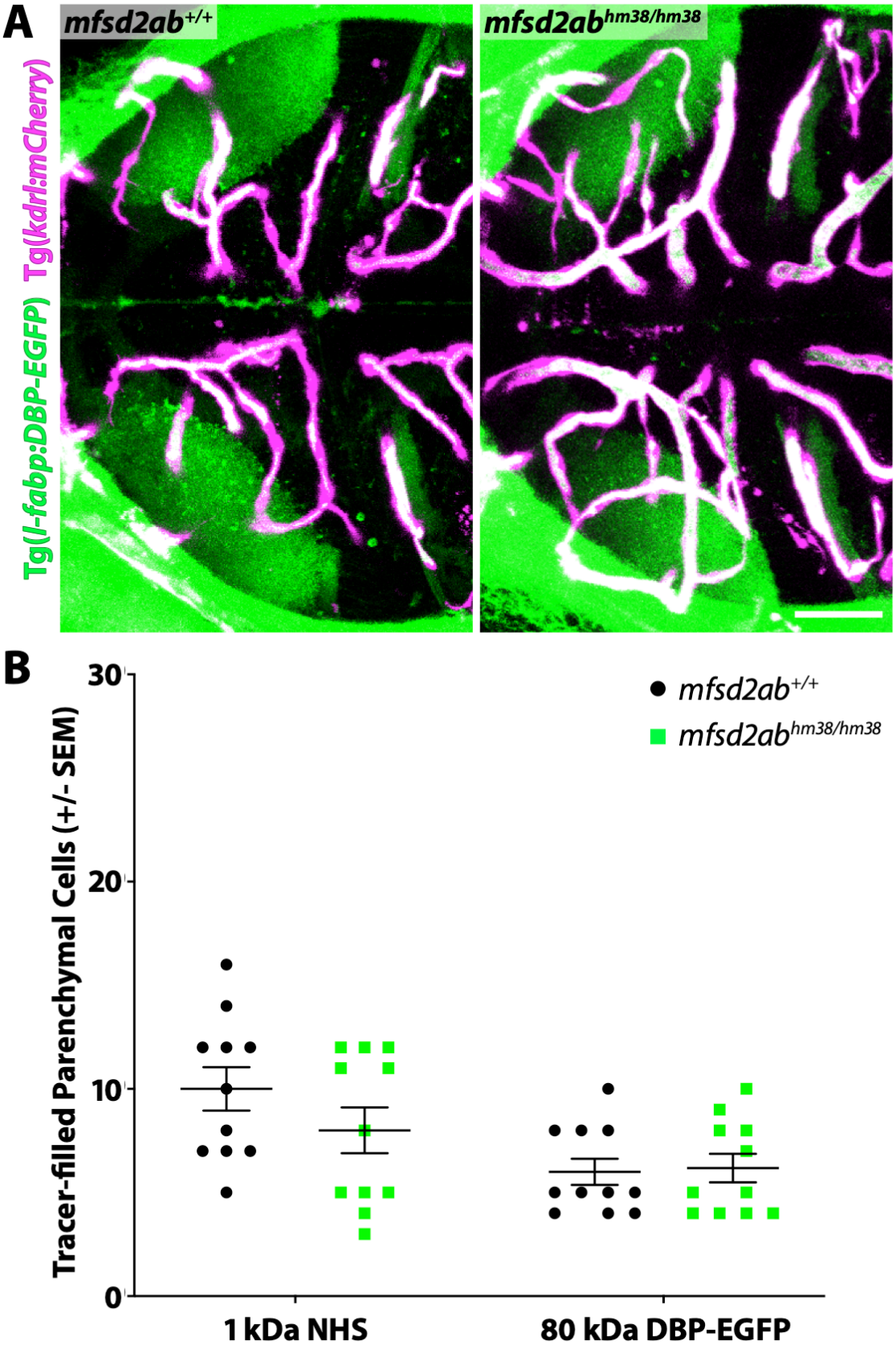
A
mfsd2ab+/+
mfsd2abhm38/hm38
Tg(kdrl:mCherry)
Tg(l-fabp:DBP-EGFP)
B
mfsd2ab+/+
mfsd2abhm38/hm38
Tracer-filled Parenchymal Cells (+/- SEM)
30
20
10
0
1 kDa NHS
80 kDa DBP-EGFP

717

718 **Figure 4 - Supplement 2. *Mfsd2ab* mutants do not have altered BBB permeability.** (A)
719 Representative maximum intensity projection images of the midbrain of wildtype and *mfsd2ab*
720 mutants expressing the fluorescently labelled 80 kDa transgenic serum protein DBP-EGFP
721 (green) at 5 dpf. *Mfsd2ab* mutants have a similarly low number of DBP-EGFP-filled parenchymal
722 cells compared to wildtype siblings. The scale bar represents 50 μm. (B) Quantification of tracer-
723 filled (NHS and DBP-EGFP) parenchymal cells in the midbrain of wildtype (black) and *mfsd2ab*
724 mutants (green). *Mfsd2ab* mutants display no significant barrier permeability defects, both for the
725 injected NHS and the endogenous transgene DBP-EGFP (A). Each individual fish measured is
726 displayed as a single point. The mean and the standard error are drawn in black.

A
mfsd2aa+/+; mfsd2ab+/+
B
mfsd2aahm37/hm37; mfsd2ab+/+
C
mfsd2aa+/+; mfsd2abhm38/hm38
D
mfsd2aahm37/hm37; mfsd2abhm38/hm38
E
DBP-filled Parenchymal Cells (+/- SEM)
30
20
10
0
****
****
mfsd2aa+/+; mfsd2ab+/+
mfsd2aahm37/hm37; mfsd2ab+/+
mfsd2aa+/+; mfsd2abhm38/hm38
mfsd2aahm37/hm37; mfsd2abhm38/hm38

728 **Figure 4 - Supplement 2. *Mfsd2aa$^{hm37/hm37}$; mfsd2ab$^{hm38/hm38}$* double mutants display similar**
729 **increased BBB permeability to *mfsd2aa$^{hm37/hm37}$* fish.** (A-D) Representative maximum intensity
730 projection images of the midbrain of wildtype (A; *mfsd2aa$^{+/+}$; mfsd2ab$^{+/+}$*), *mfsd2aa$^{hm37/hm37}$* single
731 mutants (B), *mfsd2ab$^{hm38/hm38}$* single mutants (C), and *mfsd2aa$^{hm37/hm37}$; mfsd2ab$^{hm38/hm38}$* double
732 mutants (D) expressing the fluorescently labelled 80 kDa transgenic serum protein DBP-EGFP
733 (green) at 5 dpf. *Mfsd2aa$^{hm37/hm37}$; mfsd2ab$^{hm38/hm38}$* double mutants display a similar level of
734 increased tracer-filled parenchymal cells (yellow arrowheads) to the *mfsd2aa$^{hm37/hm37}$* single
735 mutants. The scale bar represents 50 μm. (E) Quantification of DBP-EGFP-filled parenchymal
736 cells in the midbrain of wildtype (black), *mfsd2aa$^{hm37/hm37}$* mutants (magenta), *mfsd2ab$^{hm38/hm38}$*
737 mutants (turquoise), and *mfsd2aa$^{hm37/hm37}$; mfsd2ab$^{hm38/hm38}$* double mutants (green). Each
738 individual fish measured is displayed as a single point. The mean and the standard error are
739 drawn in black. **** $p < 0.0001$.
740

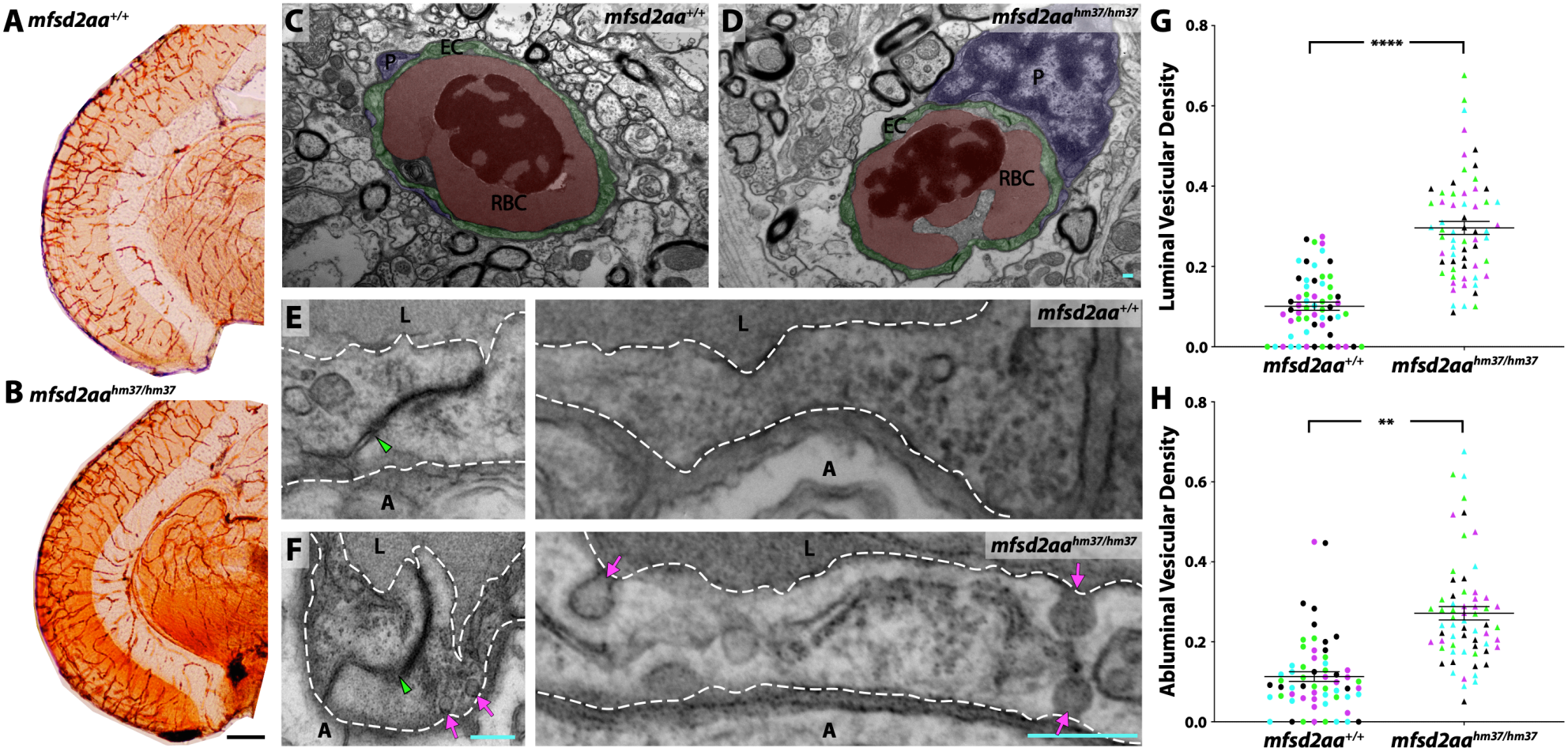
A mfsd2aa+/+
B mfsd2aahm37/hm37
C
mfsd2aa+/+
P
EC
RBC
D
mfsd2aahm37/hm37
P
EC
RBC
E
L
A
mfsd2aa+/+
L
A
F
L
A
mfsd2aahm37/hm37
L
A
G
Luminal Vesicular Density
0.0
0.2
0.4
0.6
0.8
****
mfsd2aa+/+
mfsd2aahm37/hm37
H
Abluminal Vesicular Density
0.0
0.2
0.4
0.6
0.8
**
mfsd2aa+/+
mfsd2aahm37/hm37

743 **Figure 5. M*fsd2aa* mutants exhibit increased transcytosis.** (A and B) Coronal sections of adult
744 midbrain after 30 minutes of HRP (brown) circulation in wildtype (A) and *mfsd2aa* mutant fish (B).
745 Wildtype adults confine the HRP within the blood vessels, but *mfsd2aa* mutants leak HRP into
746 the brain parenchyma. The scale bar represents 200 μm. (C and D) TEM images of individual
747 blood vessel cross-sections of adult wildtype (C) and *mfsd2aa* mutant fish (D). Endothelial cells
748 (EC) are pseudo-colored green, pericytes (P) are pseudo-colored purple and red blood cells
749 (RBC) are pseudo-colored red. (E and F) High magnification images of endothelial cells outlined
750 with white dashed lines of wildtype (E) and *mfsd2aa* mutants (F). The images are oriented with
751 the lumen (L) on top and the ablumen (A) on the bottom. *Mfsd2aa* mutants appear to have normal
752 tight junctions (green arrowhead) but elevated levels of luminal and abluminal vesicles (magenta
753 arrows). The scale bars represent 200 nm. (G and H) Quantification of the vesicular densities
754 both on the luminal (G) and abluminal (H) side of the endothelial cells reveals that *mfsd2aa*
755 mutants have increased vesicular densities. N=4 fish, each marked with a different color, with 15
756 blood vessels quantified for each fish. **** $p < 0.0001$, ** $p < 0.01$.

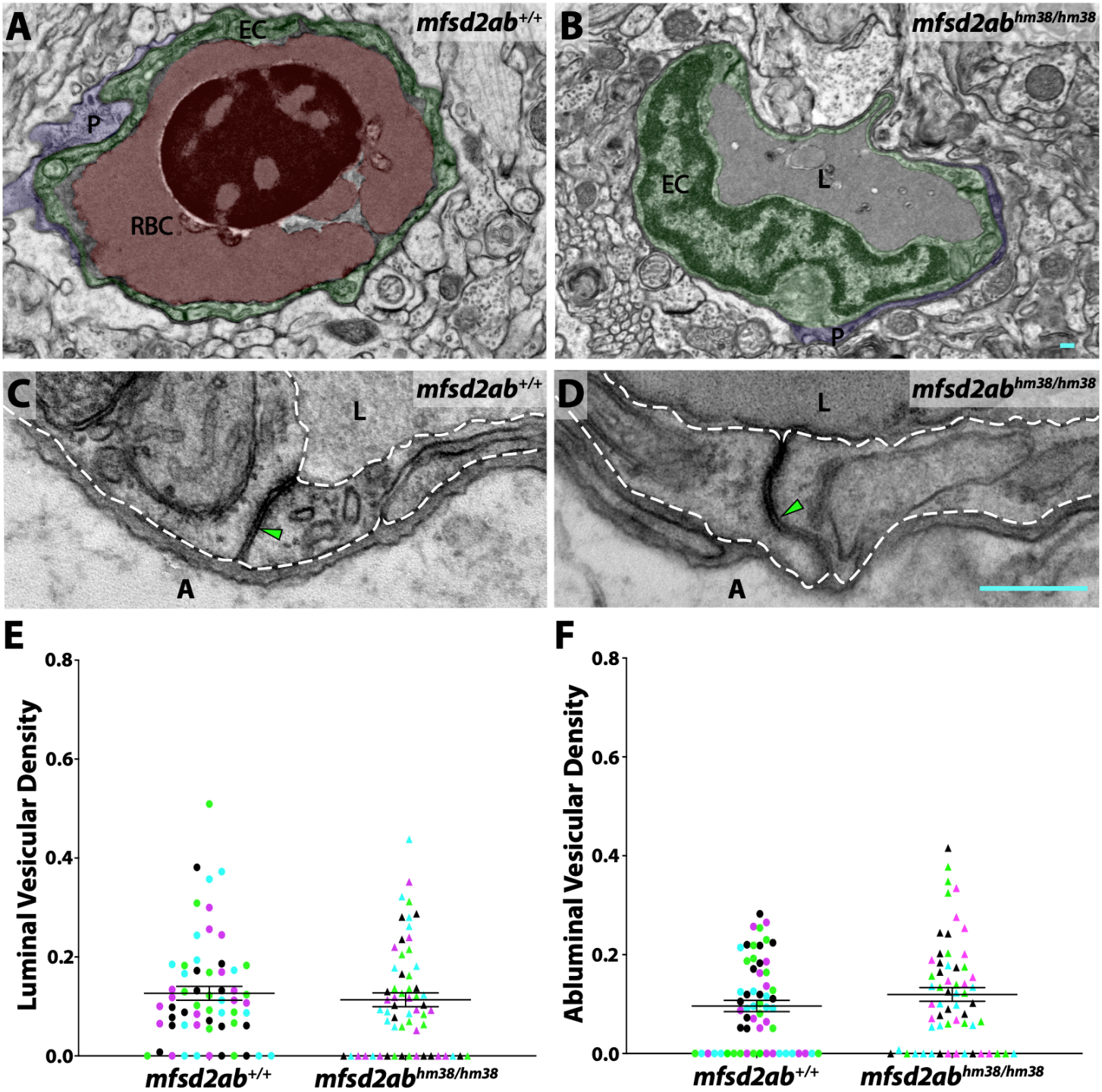
A
mfsd2ab+/+
EC
P
RBC
B
mfsd2abhm38/hm38
EC
L
P
C
mfsd2ab+/+
L
A
D
mfsd2abhm38/hm38
L
A
E
Luminal Vesicular Density
0.8
0.6
0.4
0.2
0.0
mfsd2ab+/+
mfsd2abhm38/hm38
F
Abluminal Vesicular Density
0.8
0.6
0.4
0.2
0.0
mfsd2ab+/+
mfsd2abhm38/hm38

757

758

759 **Figure 5 - Supplement 1. M*fsd2ab* mutants exhibit normal vascular maturation.** (A and B)
760 TEM images of individual blood vessel cross-sections of adult wildtype (A) and *mfsd2ab* mutants
761 (B). Endothelial cells (EC) are pseudo-colored green, pericytes (P) are pseudo-colored purple
762 and red blood cells (RBC) are pseudo-colored red when present in the lumen (L). (C and D) High
763 magnification images of endothelial cells outlined with white dashed lines of wildtype (C) and
764 *mfsd2ab* mutants (D). The images are oriented with the lumen (L) on top and the ablumen (A) on
765 the bottom. *Mfsd2ab* mutants appear to have normal tight junctions (green arrowhead) and levels
766 of luminal and abluminal vesicles. The scale bars represent 200 nm. (E and F) Quantification of
767 the vesicular densities both on the luminal (E) and abluminal (F) side of the endothelial cells
768 reveals that *mfsd2ab* mutants have similar vesicular densities to wildtype siblings. N=4 fish, each
769 marked with a different color, with 15 blood vessels quantified for each fish.